

C: Surfaces, Interfaces, Porous Materials, and Catalysis

Screening Diffusion of Small Molecules in Flexible Zeolitic Imidazolate Frameworks Using a DFT Parameterized Force Field

Ross J. Verploegh, Ambarish Kulkarni, Salah Eddine Boulfelfel, Jonathan C. Haydak, Dai Tang, and David S. Sholl

J. Phys. Chem. C, **Just Accepted Manuscript** • DOI: 10.1021/acs.jpcc.9b00733 • Publication Date (Web): 06 Mar 2019

Downloaded from <http://pubs.acs.org> on March 12, 2019

Just Accepted

"Just Accepted" manuscripts have been peer-reviewed and accepted for publication. They are posted online prior to technical editing, formatting for publication and author proofing. The American Chemical Society provides "Just Accepted" as a service to the research community to expedite the dissemination of scientific material as soon as possible after acceptance. "Just Accepted" manuscripts appear in full in PDF format accompanied by an HTML abstract. "Just Accepted" manuscripts have been fully peer reviewed, but should not be considered the official version of record. They are citable by the Digital Object Identifier (DOI®). "Just Accepted" is an optional service offered to authors. Therefore, the "Just Accepted" Web site may not include all articles that will be published in the journal. After a manuscript is technically edited and formatted, it will be removed from the "Just Accepted" Web site and published as an ASAP article. Note that technical editing may introduce minor changes to the manuscript text and/or graphics which could affect content, and all legal disclaimers and ethical guidelines that apply to the journal pertain. ACS cannot be held responsible for errors or consequences arising from the use of information contained in these "Just Accepted" manuscripts.



ACS Publications

is published by the American Chemical Society, 1155 Sixteenth Street N.W., Washington, DC 20036

Published by American Chemical Society. Copyright © American Chemical Society. However, no copyright claim is made to original U.S. Government works, or works produced by employees of any Commonwealth realm Crown government in the course of their duties.

Screening Diffusion of Small Molecules in Flexible Zeolitic Imidazolate Frameworks Using a DFT Parameterized Force Field

Ross J. Verploegh¹, Ambarish Kulkarni², Salah Eddine Boulfelfel¹,
Jonathan C. Haydak¹, Dai Tang¹, David S. Sholl^{1,*}

*¹School of Chemical & Biomolecular Engineering, Georgia Institute of Technology,
Atlanta, GA 30332-0100*

*²SUNCAT Center for Interface Science and Catalysis, Department of Chemical Engineering,
Stanford University, 450 Serra Mall, Stanford, California 94305*

***CORRESPONDING AUTHOR:** david.sholl@chbe.gatech.edu

ABSTRACT

Quantitatively modeling adsorbate diffusion through zeolitic imidazolate frameworks (ZIFs) must account for the inherent flexibility of these materials. The lack of a transferable intramolecular ZIF force field (FF) for use in classical simulations has previously made accurate simulation of adsorbate diffusion in many ZIFs impossible. We resolve this problem by introducing a density functional theory (DFT) parameterized force field (FF) for ZIFs named the intraZIF-FF, which includes perturbations to the class I force fields previously used to model ZIFs. This FF outperforms ad hoc force fields at predicting ab initio relative energies and atomic forces taken from fully periodic ab initio molecular dynamics (MD) simulations of SALEM-2, ZIF-7, ZIF-8, and ZIF-90. We use the intraZIF-FF to predict the infinite dilution self-diffusion coefficients of thirty adsorbates with molecular diameters ranging from 2.66 to 7.0 Å in these four ZIFs. These results greatly increase the number of adsorbates for which accurate information about molecular diffusion in ZIFs is available.

1. INTRODUCTION

Although metal-organic frameworks (MOFs)¹ have potential for use in molecular sieving², catalytic³, liquid separation⁴, gas adsorption and storage⁵, electronic⁶, and sensing⁷ applications, better engineering of MOF-based applications requires atomic-scale insight. MOFs are neither static nor rigid nanoporous materials. Coudert et al. classified the flexibility of MOFs that occurs upon thermal activation, pressure-induced strain, and adsorbate loading.⁸ Flexibility categories include intraframework dynamics, negative thermal expansion, swelling, breathing, gate opening, and topology-conserving metastable phase transitions. Some especially notable MOFs demonstrating these behaviors include zeolitic imidazolate frameworks (ZIFs), a chemically and thermally stable family of MOFs.⁹ Representative examples of ZIF flexibility include, but are certainly not limited to, ZIF-4, ZIF-7, ZIF-8, and ZIF-90. ZIF-4 undergoes a reversible phase transition upon cooling through a cooperative rotation of the imidazolate linkers.¹⁰ ZIF-7 exhibits a phase transition upon thermal activation¹¹ and gate opening when exposed to light alkenes and alkanes.¹²⁻¹³ Tight-fitting adsorbates with kinetic diameters (> 4.5 Å), larger than the pore limiting diameter (PLD) of ZIF-8 (3.4 Å), can enter the cavities of ZIF-8 due to the flexibility of the framework's 2-methylimidazolate linkers.¹⁴ ZIF-8 and ZIF-90 both undergo a metastable phase transition upon nitrogen loading at 77 K.¹⁵

Any effort to use ZIFs or other MOFs in membranes or kinetic pressure/temperature swing adsorption relies directly on the potential for these materials to achieve diffusion-based separations.¹⁶⁻¹⁷ Any assessment of these separations requires knowledge of the diffusivities of molecules in ZIFs.¹⁸ We recently used free energy sampling methods along with a force field (FF) describing the flexibility of ZIF-8 to simulate diffusion of 15 molecules in this widely studied material¹⁹. Our results showed good agreement with experimental data over a broad range of molecular sizes, including molecules considerably larger than ZIF-8's nominal pore diameter. Including the flexibility of ZIF-8 was critical in making accurate predictions of molecular diffusion. This implies that efforts to screen libraries of materials for diffusion-based separations based on simulations in rigid materials²⁰⁻²¹ cannot be expected to be quantitative. While kinetic flexibility occurs on timescales that can be captured with ab initio simulations, adsorbate diffusion occurs on much longer timescales, thus requiring the use of classical force fields.²²⁻²³

Force fields (FFs) allowing the modeling of flexibility in several MOFs have been developed previously. Greathouse and Allendorf implemented a FF for IRMOF-1 that reproduced framework collapse upon addition of water²⁴ and used it to examine negative thermal expansion, benzene self-diffusion, vibrational frequencies, and other structural properties²⁵. They treated the intramolecular degrees of freedom (DOFs) of the benzene dicarboxylate (BDC) organic linker with the consistent valence force field (CVFF) and the Zn-O interactions with nonbonded 12-6 Lennard-Jones (LJ) and coulombic interactions. Dubbeldam et al. examined negative thermal expansion of IRMOF-1, IRMOF-10, and IRMOF-16, using a hybrid nonbonded/bonded force field similar to that of Greathouse and Allendorf.²⁶ They departed from Greathouse and Allendorf by treating the oxygen atoms in the linkers with different parameters from the oxygen atoms in the metal-oxide cluster. Salles et al. implemented a FF for MIL-53(Cr) treating the organic moiety with the CVFF and parameterized bonded Cr-O interactions, using DREIDING parameters as starting values, to reproduce structural features of the narrow and large pore structures upon energy minimization.²⁷ This FF predicted the CO₂- and temperature-induced phase transitions known for this material. Gee et al. used FFs to model the intraframework dynamics of MIL-47 and MOF-48 and demonstrated prediction of C₈ aromatic adsorption selectivity when these dynamics were included.²⁸

The studies mentioned above provided insight into MOF flexibility but the FFs are not readily applicable to other materials. Several procedures are available for obtaining force fields using, for example, empirical methods, experimental data, or theoretically calculated Hessian matrices.²⁹ In the examples above general force field parameters (e.g. the Universal force field (UFF), DREIDING, and AMBER) were modified in an *ad hoc* manner to obtain experimentally observed MOF properties. This approach leads to what can be termed empirical force fields. Recently, Coupry et al.³⁰ developed the Universal Force Field for Metal-Organic Frameworks (UFF4MOF), extending the standard UFF parameterization procedure to encompass >99% of all MOFs in the Computation-Ready Experimental (CoRE) MOF database³¹. Coupry et al. noted, however, that dynamic properties may not be well modeled using UFF4MOF making it less accurate than AMBER which we used to benchmark our intraZIF force field. An alternative is to develop a FF based on underlying quantum mechanical (QM) calculations. QM frequency-based methods have been developed that identify bonded force constants from the diagonal elements of the dynamical (i.e., Hessian) matrix. These methods can be sensitive to the choice of internal

coordinates.³² Other methods include potential energy and force matching of empirical potentials to ab initio molecular dynamics (AIMD) data.³³ The ForceBalance FF fitting package of Wang et al. enables a hybrid approach that combines ab initio and experimental data.³⁴

The first ab initio parameterized MOF FF was developed by Tafipolsky et al. for MOF-5,³⁵ which Amirjalayer et al. subsequently used to accurately predict the self-diffusion coefficient of adsorbed benzene³⁶. Bureekaew et al. developed a FF based purely on ab initio frequency reference data and a genetic algorithm (GA) to fit only the bonded terms, having predetermined the non-bonded terms, for several MOF families.³⁷ Bristow et al. parameterized the so-called BTW-FF for MOFs using a Molecular Mechanics 3 (MM3) empirical potential³⁸, also with a frequency based method.³⁹ QuickFF, developed by Vanduyfhuys et al., utilizes a frequency based method with harmonic potentials describing bonded interactions.⁴⁰ Rogge et al. studied UiO-66, -67, and -68 containing missing linker defects using FFs derived from QuickFF.⁴¹

Multiple studies have modeled ZIFs using flexible FFs. Hertäg et al. performed the first molecular dynamics (MD) simulation of flexible ZIF-8 using the DREIDING and AMBER FFs, demonstrating that flexibility was important in predicting the diffusion of H₂ and CH₄.⁴² Battisti et al. made self-diffusion predictions for CO₂, CH₄, N₂, and H₂ in ZIF-2, -4, -5, -8, and -9 using the DREIDING FF but no charges to model flexibility.⁴³ Thornton et al. examined seven ZIF materials for the separation of H₂, CO₂, N₂, and CH₄, modeling ZIF flexibility with the DREIDING force field.⁴⁴ Zheng et al. used the AMBER-FF to model ZIF-8 with atomic charges and more accurately predicted CO₂ self-diffusion as a function of loading.⁴⁵ Gee et al. studied small alcohol diffusion in ZIF-8 and ZIF-90, comparing the AMBER and DREIDING FFs.⁴⁶ Zhang et al. introduced a ZIF-8 FF comprised of AMBER parameters with specifically tuned N-Zn-N-C proper dihedrals to reproduce the reversible structural transition upon high N₂ loading at 77 K.⁴⁷ Chokbunpiam et al. used the Hertäg's AMBER version of the ZIF-8 FF to predict ethane diffusion.⁴⁸ Krokidas et al. parameterized a harmonic ZIF-8 and ZIF-67 FF using a frequency based method for stretching and bending terms and AMBER parameters for the dihedrals.⁴⁹ Du et al. extended Zhang et al.'s ZIF-8 FF to treat the temperature-induced reversible phase change of ZIF-7.¹¹ Phuong et al. used the AMBER and DREIDING variants of the ZIF-90 FF proposed by Gee et al. to predict CH₄ diffusion in ZIF-90.⁵⁰ Gao et al. proposed a coarse-grained FF and studied pressure and temperature induced structural changes for various ZIF structures.⁵¹

In most cases, the ZIF FFs described above were developed based on a limited set of structural properties. In this paper, we introduce a flexible ZIF force field we refer to as the intraZIF-FF using data from a diverse set of density functional theory (DFT) calculations of static and dynamic ZIFs. We added perturbations to the traditional class I ZIF force fields via a Morse potential describing Zn-N bonds and a 3-term Fourier series describing N-Zn-N-C proper torsions. We make thorough comparisons of our intraZIF-FF to the AMBER-FF for various ZIF properties. We then use the intraZIF-FF to predict the self-diffusivities at room temperature of thirty adsorbates with molecular diameters ranging from 2.66 to 7.0 Å in four chemically distinct ZIFs with the SOD topology, SALEM-2, ZIF-7, ZIF-8, and ZIF-90. For the majority of adsorbates we examined, there exists no prior experimental or predicted diffusion data. Our results therefore greatly expand the number of examples for which diffusivities are available. For the four ZIFs studied, simple geometric arguments would suggest that the suitability of these materials as molecular sieves would be approximately comparable. Our results show, however, that local chemical structure differences arising from flexibility as well as the interaction of adsorbates in the ZIF windows lead to drastically different diffusion characteristics. Our study provides an example of screening diffusion quantitatively in a variety of ZIF materials, aiding the identification of kinetic chemical separations where ZIFs may be useful.

2. SIMULATION METHODS

2.1 intraZIF Force Field Design and Parameterization

Our ab initio derived class I intraZIF-FF is intended to represent all degrees of freedom (DOF) in an adsorbate-free ZIF and uses the general form

$$E_{\text{intraZIF}} = \sum E_{\text{stretch}} + \sum E_{\text{bend}} + \sum E_{\text{proper}} + \sum E_{\text{coul}} + \sum E_{\text{vdW}} \quad (1)$$

Bonded potentials include stretching and bending modes and proper dihedrals. Nonbonded potentials include electrostatic interactions through assignment of point charges and van der Waals interactions through a Buckingham potential. Fitting of bond and angle parameters was performed through a frequency-based method while proper dihedral parameters were fit according to a potential energy matching; both using QM cluster calculations. Representation of metal-linker interactions is challenging since there are substantial polarization effects from the charge on the metal ions as well as changes in the coordination sphere.⁵² Metal-linker interactions can be described by bonded, nonbonded, and semi-bonded approaches, each

approach having certain advantages and limitations.⁵³⁻⁵⁴ The intraZIF-FF neglects local polarization effects and charge transfer, which could potentially better describe Zn-imidazolate interactions.⁵⁵ A comparison of intraZIF-FF parameters to the AMBER-FF parameters and additional information is reported in the Supporting Information (**Tables S.1, S.2, S.3, and S.4**).

2.1.a From Bulk Structure to Cluster Models

Here we describe our method for creating clusters representing the parent ZIFs. The experimentally determined crystal structures with disorder resolved and solvent removed were taken from the Cambridge Structural Database (CSD) with the following structure identifiers⁵⁶: ZIF-7 (Park et al., *VELVIS*)⁵⁷, ZIF-8 (Park et al., *VELVOY*)⁵⁷, ZIF-90 (Morris et al., *WOJGEI*)⁵⁸, and SALEM-2 (Hupp et al., *IMIDZB10*)⁵⁹. The geometries of these four bulk ZIF structures were energy minimized using plane wave density functional theory (DFT) as implemented in the Vienna Ab initio package (VASP),⁶⁰⁻⁶¹ version VASP5.3.5, using the PBE-GGA⁶² functional with D2 dispersion corrections⁶³. We also energy minimized all periodic structures with the D3(BJ) dispersion correction including damping.⁶⁴⁻⁶⁵ Reciprocal space was sampled at the Γ -point and all calculations used a 700 eV energy cutoff. Atomic forces were converged to < 0.03 eV/Å for both unit cell and atomic position relaxations.

Using these energy-minimized parent structures, clusters of the form $[\text{Zn}_2(\text{xIm})_7]^{3-}$ were excised containing a central imidazolate linker and the 6 nearest neighbor (NN) linkers that share the two common Zn atoms. Terminal hydrogens were not added to balance charge following a similar procedure by Krokidas et al.^{49, 66} The atomic positions of these clusters were energy minimized using VASP with the PBE functional without D2 corrections with an energy cutoff of 400 eV with an atomic force convergence of < 0.01 eV/Å. For clusters, interaction energies are dominated by bond stretching and angle bending terms. These short-range interactions are described with good accuracy using DFT PBE-GGA level of theory without applying dispersion correction. However, dispersion correction is included for long-range van der Waals interactions as explained in Section 2.1.d. A cubic $25 \times 25 \times 25$ Å supercell was used for the imidazolate (Im), imidazolate-2-carboxaldehyde (ImCA), and 2-methylimidazolate (mIm) clusters while a cubic $30 \times 30 \times 30$ Å supercell was used for benzimidazolate (BzIm) clusters. These VASP settings were also applied to the potential energy scans described below. **Figure 1** shows the four energy minimized clusters containing the Im, BzIm, ImCA, and mIm linkers. Atomic charges on the clusters were assigned using the Density Derived Electrostatic and Chemical (DDEC3) method

of Manz et al.⁶⁷⁻⁶⁸ As shown in the Supporting Information (**Figures S.14, S.15, S.16, and S.17**), the charges on the central linker in these clusters were similar to those from the bulk structures.

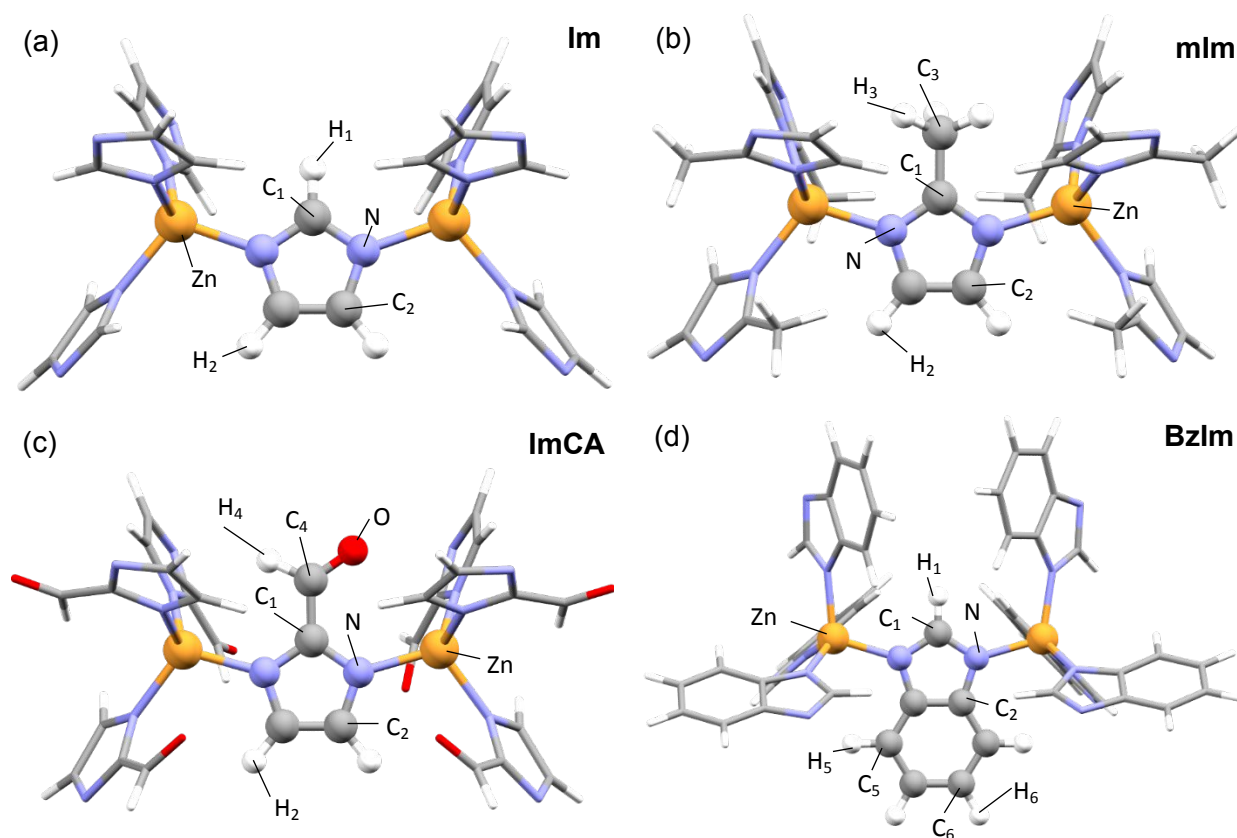


Figure 1. Cluster models for the (a) imidazolate (Im), (b) 2-methylimidazolate (mIm), (c) imidazolate-2-carboxaldehyde (ImCA), and (d) benzimidazolate (BzIm) linkers. C, N, H, O, and Zn atoms represented by grey, purple, off-white, red, and gold spheres. Each of the atom types are labelled according to their unique atomic charges.

2.1.b Stretching and Bending Modes

The Seminario method, based on the Cartesian Hessian matrix, was used for determining bond and angle force constants.³² Hessian matrices were generated using the finite difference method implemented in VASP using two displacements of 0.005 Å on either side of the minimum. Only translational DOF of atoms associated with the central linker and the tetrahedral metal centers (i.e. two Zn's and the three N's on terminal linkers) were probed. The resulting bonding and angle force constants are reported in the Supporting Information.

Bonds and angles with low spring constants are indicative of anharmonic character and are poorly described by harmonic functions. The Zn-N coordination has a harmonic spring

constant of 67.16 kcal mol⁻¹ Å⁻² for the mIm cluster according to the Seminario method. The ZIF-8 FFs of Zheng et al. and Zhang et al. use spring constants of 78.5 kcal mol⁻¹ Å⁻² and 86.0 kcal mol⁻¹ Å⁻², respectively. To better understand the Zn-imidazolate interactions and determine which interactions were poorly approximated with harmonic potentials, Born-Oppenheimer molecular dynamics (BOMD) on the fully periodic parent ZIFs were carried out using CP2K (version 2.6)⁶⁹. Energies and forces were computed with DFT as implemented in the module QUICKSTEP⁷⁰. In these calculations, the self-consistent field (SCF) minimizer was based on the orbital transformation method⁷¹, and a mixed Gaussian and Plane-Wave (GPW) method⁷²⁻⁷³ was used in combination with PBE⁶² Goedecker-Teter-Hutter (GTH) pseudopotentials⁷⁴⁻⁷⁵. The plane wave and DZVP-MOLOPT-GTH auxiliary basis set cutoffs used for SALEM-2, ZIF-7, and ZIF-8 were 550 and 70 Ry, respectively. 600 and 70 Ry cutoffs were used for ZIF-90 due to the presence of oxygen atoms. The dispersion correction DFT-D3 with damping from Becke and Johnson⁶⁴ (BJ) was applied to all simulations with a cutoff of 16 Å. First-principles molecular dynamics (MD) simulations were propagated for the four ZIF structures at 700 K and 1 bar in the NPT ensemble using the Nosé-Hoover thermostat⁷⁶ and a time-step of 1 fs. Additional NPT BOMD simulations were performed at 1 bar and 308.15 and 500 K for ZIF-90 as well as 100, 200, 300 and 500 K for SALEM-2. In all BOMD simulations, the simulation volume was a unit cell of the structure with periodic boundary conditions (PBC). This defined a simulation volume containing 204, 522, 276, and 252 atoms for SALEM-2, ZIF-7, ZIF-8, and ZIF-90, respectively. To clarify, only VASP calculations on the clusters were used to fit the intraZIF-FF to maintain consistency while CP2K was used to explore the “long time” flexibility of the periodic ZIFs.

The mean of the Zn-N bond length is temperature-dependent (**Figure S24a**) indicating that an anharmonic description is needed. To this end, we parameterized a Morse potential

$$E_{\text{Zn-N},ij} = \sum D_e (1 - e^{-\alpha(r_{ij} - r_{ij}^0)})^2 \quad (2)$$

where D_e is the depth of the potential well, α is the stiffness parameter, and r_{ij}^0 is the equilibrium bond distance. A potential energy (PE) scan was performed along the Zn-N bond on the cluster for bond lengths from 1.8-2.6 Å. The total differential energy determined from the PE scan with the energy minimized cluster as the reference state was decomposed into three contributions:

$$\Delta E_{\text{total}}^{\text{PBE}} = \Delta E_{\text{bond}} + \Delta E_{\text{electrostatic}} + \Delta E_{\text{vdW}} \quad (3)$$

Here, dispersion contribution is accounted for using vdW interactions taken from MM3 FF and MOF FF as discussed below in Section 2.1.d. To decompose the total differential PBE energy between the bonded and electrostatic contributions, LAMMPS⁷⁷ was used to determine the electrostatic contribution using the tags coul/cut with a cutoff of 25 Å and special bonds in a 50×50×50 Å supercell. Pairs of atoms separated by one, two, and three consecutive bonds (1-4 interactions) were excluded from pair interactions. Charges were obtained for atoms in the clusters using the DDEC3 method. Small deviations from the energy minimized structure were found to have a negligible electrostatic contribution to the PBE potential energy (**Figures S.1b, S.5b, S.7b, and S.10b**). We therefore assumed for simplicity that $\Delta E_{total}^{PBE} \approx \Delta E_{bond}$. The bond dissociation energies were not treated as a fitting parameter. Instead, the four clusters were cleaved along a Zn-N bond with the N on the central linker; this yielded two fragments termed “large” and “small”. An energy minimization was performed for both fragments according to the methods described already. Bond dissociation energies were determined as:

$$D_e = E_{cluster}^{PBE} - (E_{large_frag}^{PBE} + E_{small_frag}^{PBE}) \quad (4)$$

The resulting bond dissociation energies, stiffness parameters, and equilibrium bond lengths for all the clusters are reported in the Supporting Information.

The spring constants for N-Zn-N and Zn-N-C angles were also found to be low. While the histograms of the N-Zn-N angle distributions for ZIF-90 in **Figure S24b** imply that a harmonic potential is the appropriate functional form, the N-Zn-N and Zn-N-C were reparametrized using fits to potential energy scans using

$$\Delta E_{total}^{PBE} = \sum \Delta E_{angle} + \Delta E_{coul} + \Delta E_{vdW} \quad (5)$$

Similar to the Zn-N bond fitting procedure, we assume for simplification that $\Delta E_{total}^{PBE} \approx \sum \Delta E_{angle}$. The fitting procedure yields lower spring constants ($\sim 18 \text{ kcal mol}^{-1} \text{ deg}^{-2}$) than the Seminario method ($\sim 37 \text{ kcal mol}^{-1} \text{ deg}^{-2}$), probably due to imprecision in the calculation of the Hessian for these modes in the DFT data underlying our application of the Seminario method. This observation highlights the importance of carefully parameterizing the ‘softer’ DOFs.

2.1.c Dihedrals and Improper Torsions

To obtain relevant configurations and potential energies for fitting dihedral parameters, BOMD simulations of the clusters in the NVT ensemble were performed using VASP allowing

only the DOF on the central linker and the two Zn atoms to move with a Nosé-Hoover thermostat, a 1.0 fs time step and an energy cutoff of 400 eV. Using only the cluster rather than the full unit cell greatly reduces the number of dihedrals involved in our fitting. All dihedrals were parameterized during this step of the force field design, not just the dihedrals associated with the Zn-imidazolate interaction. Using MD simulations of the cluster allowed for sampling and fitting of all these dihedrals simultaneously. BOMD simulations of the clusters were performed at 100, 300, 500, and 700 K to access a representative range of relative energies (**Figures 2a and 2b insets**).

When determining our quality of fit as well as comparing the AMBER and intraZIF FFs, we report the mean absolute error (MAE), root mean squared deviation (RMSD), and mean signed difference (MSD). We also include a normalized root mean squared deviation (NRMSD)

$$NRMSD = 100 \left(\frac{RMSD}{\sigma_{QM}} \right) \quad (6)$$

where the RMSD is calculated between the MM and QM energies and σ_{QM} is the standard deviation of the QM energies. As a heuristic, an NRMSD approaching ~20% has been identified as acceptable for a force field utilizing fixed point charges.⁷⁸

We used a potential energy matching procedure of Guvench and Mackerell⁷⁹ to determine the force constants for the proper dihedrals. No improper dihedrals are included in the intraZIF-FF. We assumed that the PBE relative energies for each cluster include only stretching, bending, proper dihedrals, and Coulombic interactions. LAMMPS was used to determine the classical FF contribution of the stretching, bending, and Coulombic terms and the difference between the PBE and these FF energies was attributed to the proper dihedrals. A simulated-annealing Monte Carlo procedure with exponential cooling was used to fit a Fourier series for each dihedral (e.g. 59 dihedrals for the Im cluster).⁷⁹ The optimization protocol used a starting temperature of 5000 K with four 0.5×10^6 -step simulated-annealing runs, and spring constant constraint of [0.0, 4.5] kcal mol⁻¹ with fixed phase angles. For the imidazolate ring dihedrals, the multiplicity (i.e. number of energy minima) of the Fourier series was fixed at 2 for the imidazolate ring dihedrals while the N-Zn-N-C dihedrals had multiplicities of 1, 2, and 3. The optimized spring constants are given in **Tables S.1, S.2, S.3, and S.4**. As a representative example, the RMSD and NRMSD for the Im cluster was 8.90 kJ mol⁻¹ and 26.8% before the inclusion of any proper dihedrals and 7.06 kJ/mol and 21.3% after inclusion of the dihedrals.

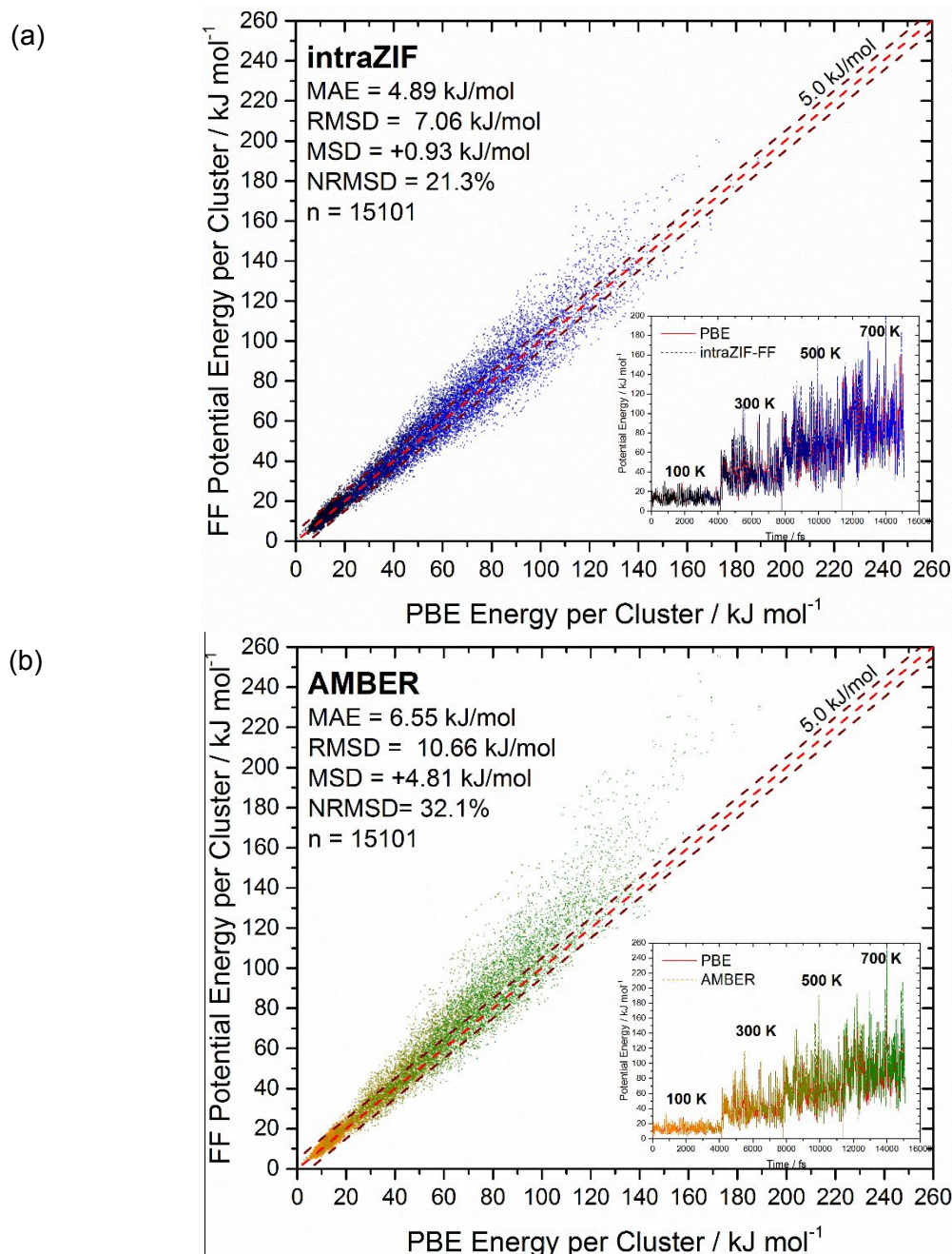


Figure 2. Relative energy comparisons between PBE and (a) the intraZIF-FF including Fourier dihedrals from the potential energy fitting and (b) the AMBER-FF using standard cosine proper dihedrals for the Im cluster. Insets represent the concatenated relative energy time series for the simulations with increasing temperature. The color code (black to blue/intraZIF and orange to green/AMBER) is designed to easily identify the low and high energy regions.

Figure 2 compares the PBE energies with the intraZIF-FF and AMBER-FF for the BOMD simulations in VASP on the Im cluster. The NRMSD for the AMBER-FF is greater at 32.1%, showing the intraZIF-FF (NRMSD = 21.3%) better represents relative energies. Closer examination of low energies ($< 20 \text{ kJ mol}^{-1}$) reveals that the two FFs represent low energies with similar accuracy (**Figure S4**). Similar plots for the BzIm, mIm, and ImCA clusters are in the Supporting Information (**Figures S.6, S.8, and S.11**). For all clusters, there is a systematic improvement in computing relative high energies. This is very important to describe ZIF materials under changes in temperature (Figure S21 for temperature dependence of SALEM-2 cell volume) or external pressure (See Section 3.2 for pressure dependence of the ZIF-8 unit cell parameters). The relative energies and forces are also in better agreement with BOMD (see Section 3.3).

In **Section 3** we also compare the intraZIF and AMBER FFs to fully periodic BOMD data that, unlike the BOMD data for clusters, was not used to fit the intraZIF-FF.

2.1.d van der Waals and Coulombic Interactions

Intraframework van der Waals interactions were modeled using a Buckingham potential

$$E_{\text{vdW},ij} = Ae^{-r_{ij}/\rho} - \frac{C}{r_{ij}^6} \quad (7)$$

Following the MM3 FF⁸⁰, the three parameters in the Buckingham potential correspond to an energy parameter ϵ_{ij} and the sum of the vdW radii of the two interacting atoms r_{ij}^0 :

$$A = 1.84 \times 10^5 \epsilon_{ij}, \rho = \frac{r_{ij}^0}{12}, C = 2.25 \epsilon_{ij} (r_{ij}^0)^6 \quad (8)$$

The vdW parameters in the intraZIF-FF are reported in **Table S5** as adapted from the MM3 FF as well as the MOF-FF by Bureekaew et al.³⁷ The accuracy of potential curves corresponding to these vdW parameters is very comparable to quantum mechanics reference computed by dispersion-corrected double-hybrid functional B2PLYP+D.³⁷ Grimme and Steinmetz have shown that B2PLYP-D level of theory outperforms 15 other DFT, HF, MP2, and semi-empirical methods for dispersion correction in common organic structural motifs.⁸¹

Coulombic interactions were modeled using a hybrid approach rather than standard Ewald summation since it was found to reproduce the experimental lattice constants from fully periodic molecular dynamics simulations. Specifically, some atomic interactions were

represented with a standard Coulombic interaction potential and others with a Debye damping factor added to the Coulombic interaction:

$$E_{\text{coul},ij} = \frac{Cq_iq_j}{\epsilon r_{ij}} \quad \text{and} \quad E_{\text{Debye},ij} = \frac{Cq_iq_j}{\epsilon r_{ij}} e^{-\kappa r_{ij}} \quad (9)$$

The Debye length κ is set to 0.33 \AA^{-1} . If a pair of atoms was separated by 3 consecutive bonds (1-4 interactions) and the electrostatic interaction of the pair was modeled using the Coulombic interaction potential with the Debye damping parameter, their 1-4 electrostatic interaction was included (i.e. scaling factor of 1.0) in the calculation of the potential energy and atomic forces.

We selected specific pairs of interactions to be described with Debye damping to obtain < 1.0% error between the experimental unit cell volume and the volume predicted by the intraZIF-FF. These specific interactions only include Zn-Zn and Zn- X_{organic} interactions, where X_{organic} =H, C, N, or O. Setting these interactions was performed through a targeted trial-and-error procedure during which attractive (repulsive) Coulombic interactions are treated with a Debye interaction when the unit cell volume was greater than (less than) the experimental unit cell volume. The experimental unit cells were determined at specific temperatures and pressures as recorded in **Table 1**. We therefore performed a series of NPT-MD simulations on the empty parent ZIFs using LAMMPS with a vDW and Coulomb cutoff of 15.5 \AA and a 1.0 fs timestep to assess cell volumes from FF calculations. Cell parameters were set to fluctuate anisotropically, but the cell angles were held fixed during these simulations. Coulombic interactions utilizing the Debye damping parameter are summarized **Table S9**.

Table 1. Comparison of experimental and intraZIF predicted unit cell lattice parameters and volumes.

ZIF, Conditions	Exptl. XRD	intraZIF-FF				Volume		
	T / K, P / atm	a (c) / \AA	a / \AA	b / \AA	c / \AA	XRD V / \AA^3	FF V / \AA^3	% Error
SALEM-2	100, 1.0	16.83	16.88±0.06	16.85±0.07	16.80±0.07	4767	4778	+0.23
ZIF-7	258, 1.0	22.99 (15.76)	22.84±0.08	22.84±0.09	16.10±0.04	7214	7275	+0.84
ZIF-8	258, 1.0	16.99	16.96±0.07	16.97±0.08	16.97±0.06	4904	4883	-0.44
ZIF-90	100, 1.0	17.27	17.40±0.04	17.36±0.04	17.08±0.04	5151	5159	+0.16

2.2 Adsorbate Force Fields and ZIF-Adsorbate Interactions

We selected thirty adsorbates that exhibit various molecular sizes, shapes, and interaction strengths: He, Kr, Xe, Rn, SF₆, H₂, O₂, N₂, CO₂, CH₃OH (methanol), C₂H₅OH (ethanol), C₄H₉OH (1-butanol), CH₃-CO-CH₃ (acetone), CH₄, C₂H₄=, C₂H₆, C₃H₆=, C₃H₈, 1-C₄H₈=, n-C₄H₁₀, iso-C₄H₈=, iso-C₄H₁₀, C₆H₆, m-C₈H₁₀, o-C₈H₁₀, p-C₈H₁₀, water, N,N-dimethylformamide (DMF), imidazole, and 1,3,7-trimethylxanthine (caffeine, C₈H₁₀N₄O₂). **Figure S26** in the Supporting Information shows the molecular weights of these species as a function of their molecular diameters. The molecular diameters are a combination of previously reported van der Waals and kinetic diameters^{14, 82}; those not found in literature were approximated using the Lennard-Jones sigma parameters summed across the second shortest molecular dimension. The FFs used to define adsorbate-adsorbate interactions and adsorbate-ZIF interactions for these species are described in the Supporting Information.

2.3 Diffusion Theory and Biased Molecular Dynamics Methods

Self-diffusion of adsorbates through cage-type ZIFs can be modeled as an activated hopping process from cage to cage through connecting windows. The self-diffusion coefficient can be written as⁸³

$$D_{self} = \left(\frac{n_{windows}}{2d} \right) \kappa k_{i \rightarrow j}^{TST} \lambda^2 \quad (10)$$

where $n_{windows}$ is the number of possible windows through which an adsorbate can exit from its current cage ($n_{windows}$ = 8 for SALEM-2, ZIF-8, and ZIF-90), d takes on values of 1, 2, or 3 based on the diffusion dimensionality, (d = 3 for SALEM-2, ZIF-8, and ZIF-90), κ is the dynamical correction to the hopping rate $k_{i \rightarrow j}^{TST}$ from transition state theory (TST)⁸⁴, and λ is the cage to cage distance. An average λ of 14.75 Å was utilized for SALEM-2, ZIF-8, and ZIF-90 because of their similar unit cell parameter.

To produce the Gibbs free energy curve for calculation of the TST hopping rate, umbrella sampling calculations were performed with LAMMPS using the collective variables (COLVARS) package by Fiorin and coworkers.⁸⁵ Spring constants of 10, 25, and 50 kcal mol⁻¹ Å⁻² were used for adsorbates exhibiting small (e.g. He), medium (e.g. CH₄) and large (e.g. isobutane) diffusion barriers. Sixty umbrellas were used over the 1-dimensional reaction

coordinate with spacings of 0.25 Å. Each simulation was equilibrated for 200 ps with 500 ps of sampling during an NPT simulation. Blocking potentials were applied to constrain the molecules to the immediate two cage system, ensuring that small adsorbates only sampled the microstates of interest. The weighted histogram analysis method (WHAM) was used to combine umbrella simulations into a free energy curve.⁸⁶ Dynamical corrections were measured using the algorithm detailed by Frenkel and Smit.⁷⁶ Further details of these methods are discussed in our previous work.¹⁹

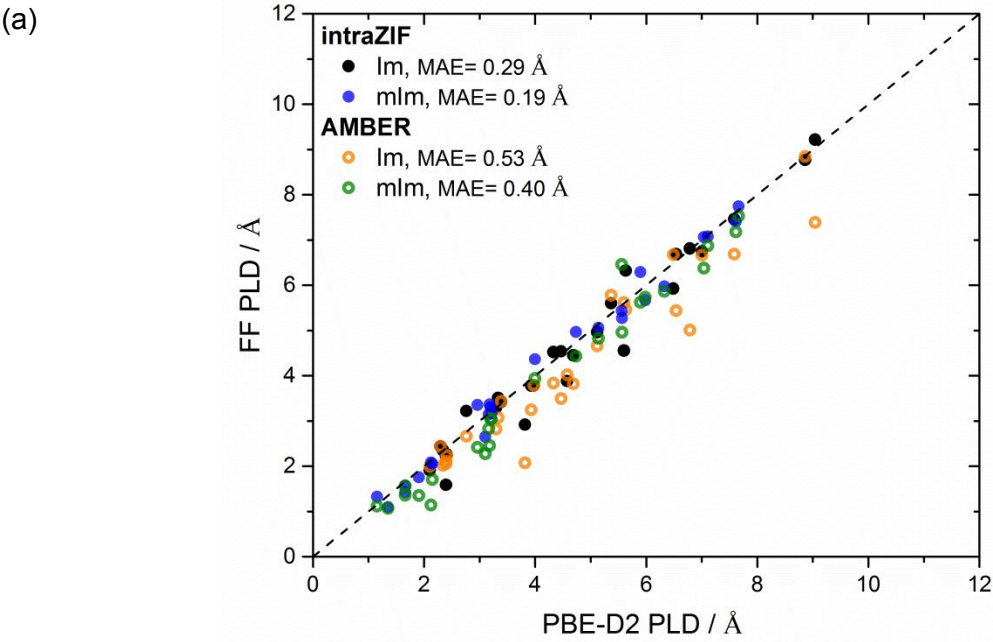
3. RESULTS AND DISCUSSION

3.1 Structural Properties of Im and mIm ZIF Polymorphs

The criteria for assessing the quality of a MOF FF can broadly be classified as static or dynamic. Typically, static properties are easier to predict and thus discussed first. To this end, we compared densities (ρ), pore limiting diameters (PLDs)²¹, largest cavity diameters (LCDs), and accessible surface areas (ASA) predicted by PBE-D2 and PBE-D3(BJ) to those predicted by the AMBER and intraZIF FFs. Energy minimizations for each FF were performed in LAMMPS using both the conjugate gradient and Hessian-free truncated Newton Raphson algorithms to relax both the unit cell parameters and atomic positions. Zeo++⁸⁷ was used to determine the PLDs, LCDs, ASAs, and AVs, with a probe radius of 1.3 Å and 10000 and 50000 Monte Carlo cycles for the ASA and AV calculations, respectively. **Tables S.10, S.11, S.12, and S.13** summarize these properties for SALEM-2, ZIF-7, ZIF-8, and ZIF-90. We find better agreement to the DFT predicted properties using the intraZIF-FF since the AMBER-FF predicts that the unit cell parameters contract significantly. We fit the intraZIF-FF to experimental lattice parameters at finite temperatures, so it is not surprising that in comparisons to energy minimized structures intraZIF-FF performs better than the AMBER-FF.

To expand the set of structures used for comparisons, we also performed energy minimizations using PBE-D2, PBE-D3(BJ), the AMBER-FF, and the intraZIF-FF for the Im and mIm versions of the hypothetical ZIF polymorphs reported by Baburin et al.⁸⁸⁻⁸⁹ Information from these two sets of polymorphs was not used to fit the intraZIF-FF. **Figure 3** compares the PLDs and ASA of the PBE-D2 energy minimized polymorphs to those of the intraZIF and AMBER energy minimized polymorphs. **Figure S18** compares the densities and LCDs. The intraZIF-FF more closely reproduces structural features of both sets of polymorphs than the AMBER-FF. For all the Im and mIm polymorphs, the AMBER-FF over predicts the densities.

Even more important for prediction of adsorption and diffusion are accurate prediction of PLDs and LCDs. The intraZIF-FF lowers the MAE for these two quantities by nearly 50%, as seen in **Figure 3**. Furthermore, several of the AMBER-FF energy minimized structures predict a zero accessible surface area for a 2.6 Å diameter spherical probe. These structures have not completely collapsed as inferred from the LCD parity plot (**Figure S18**), rather, they have PLDs smaller than the probe size. The intraZIF-FF only predicts a significantly reduced accessible surface area for the Im-*qtz* polymorph.



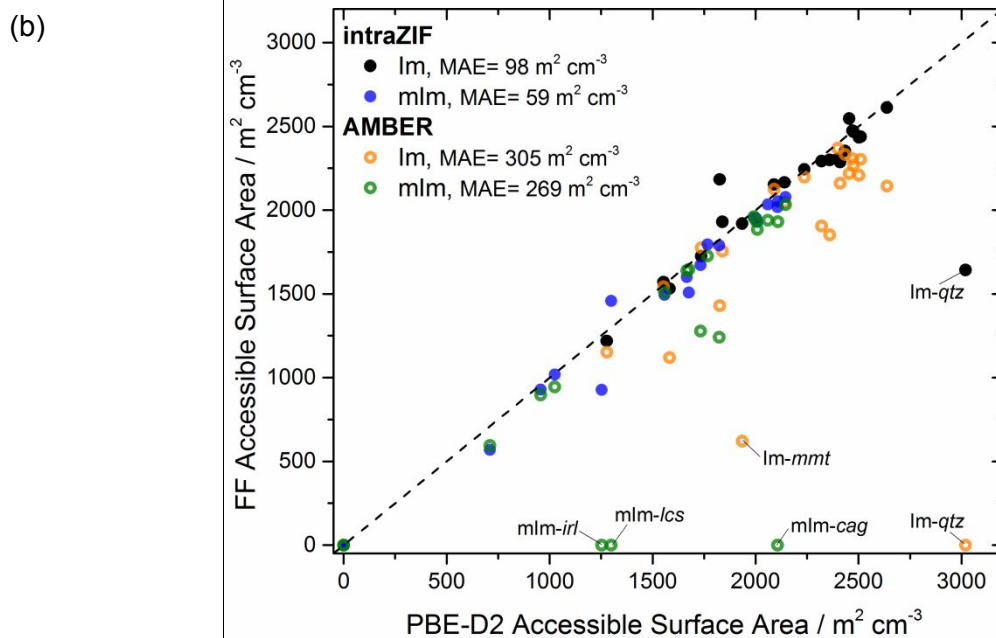


Figure 3. Parity plots for (a) PLDs and (b) accessible surface areas with a probe radius of 1.3 Å as predicted by PBE-D2 and the intraZIF (blue/black closed circles) and AMBER (orange/green) force fields. There are 27 Im polymorphs (black/orange circles) including SALEM-2 and 25 mIm polymorphs (blue/green circles) including ZIF-8.

3.2 Bulk Modulus Predictions

The ability of a force field to predict mechanical stability is another important metric. **Figure 4** shows the pressure dependence of the ZIF-8 unit cell parameters at 308 K as well as the amorphization pressure as first described by Chapman et al.⁹⁰ We define the amorphization pressure as the pressure at which the unit cell volume decreases by >25% during a 1 ns NPT-MD simulation with a 100 ps equilibration period. After structural collapse, the intraZIF-FF is assumed to not accurately capture the dynamics of forming an amorphous phase, which in real materials is likely to involve bond breaking and reformation. The intraZIF-FF captures the nonlinearity in the unit cell parameter pressure dependence and predicts an amorphization pressure range from 0.3-0.5 GPa (the experimental amorphization pressure is 0.34 GPa). The AMBER-FF predicts an amorphization pressure of > 0.6 GPa and the P-dependence of the unit cell parameters is linear. The pressure-induced changes in the unit cell parameters were fit to the third-order Birch-Murnaghan equation of state to determine the bulk modulus and the derivative of the bulk modulus:

$$K = -V \left(\frac{\partial P}{\partial V} \right)_{P=0} = \frac{\sigma_V}{\varepsilon_V} \text{ and } K' = \left(\frac{\partial K}{\partial P} \right)_{P=0} \quad (11)$$

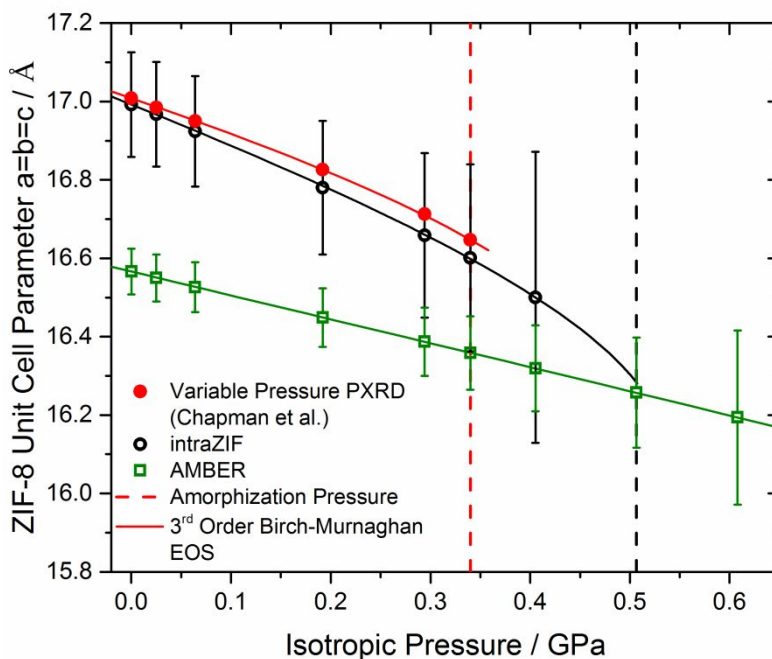


Figure 4. Pressure dependence of the ZIF-8 unit cell parameters measured by Chapman et al.⁹⁰ and predicted by the intraZIF and AMBER FFs. The third-order Birch-Murnaghan isothermal equation of state is fit (solid line) to both the measured and predicted data. The amorphization pressures are indicated by the dashed lines.

The bulk modulus and K' predicted by the intraZIF-FF and Chapman et al. are 5.53 GPa and -2.68 and 6.52 \pm 0.35 GPa and -4.6 \pm 0.14 respectively.⁹⁰ The AMBER-FF predicts a bulk modulus and K' of 9.05 GPa and -0.02. Zhang et al. using a modified version of the AMBER-FF estimated the bulk modulus as 8.37 \pm 0.05 GPa.⁴⁷

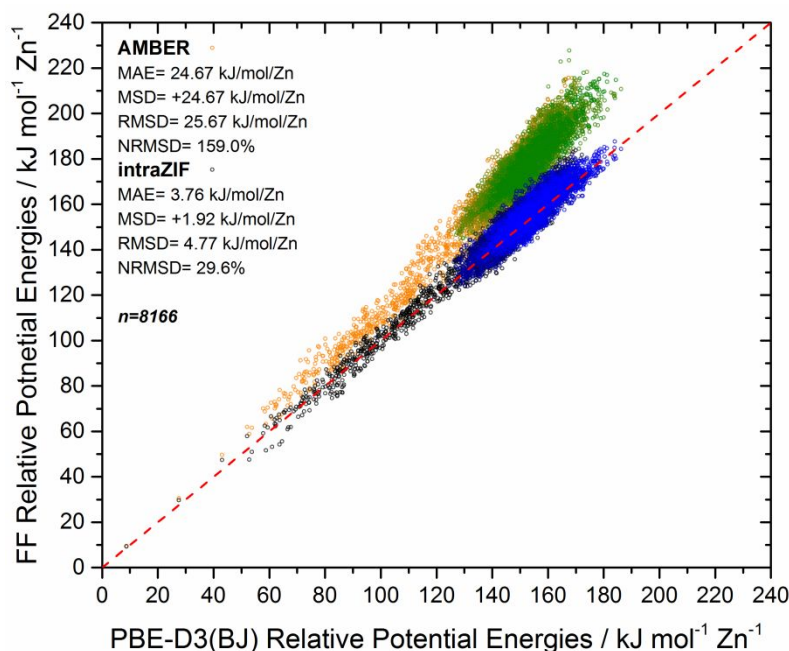


Figure 5. SALEM-2 relative potential energies as predicted by the AMBER-FF (orange to green) and intraZIF-FF (black to blue) in reference to PBE-D3(BJ) relative energies from fully periodic BOMD simulations at 700 K.

3.3 Reproducibility of Relative Energy and Forces from BOMD Calculations

The intraZIF and AMBER force fields were compared for their ability to reproduce PBE-D3(BJ) reference potential energies and atomic forces from BOMD simulations at 700 K and 1.0 bar on the full unit cells. Development of the intraZIF-FF used fitting based on BOMD data from small clusters (as described above), but the BOMD simulation data on the full unit cells was not used in fitting the intraZIF-FF. This test is different from the BOMD simulations of the clusters because these comparisons also include van der Waals pair-wise interactions. **Figure 5** compares the PBE-D3(BJ) relative energies and those predicted by the AMBER and intraZIF FFs for SALEM-2. The time series of the data is represented by the black to blue (intraZIF) and orange to green (AMBER) fade. AMBER-FF and intraZIF-FF yield NRMSDs of 159.0% and 29.6% respectively, clearly showing that the intraZIF-FF outperforms the AMBER-FF. Similar plots for ZIF-8, ZIF-90, and ZIF-7 are in **Figure S22, S.23, and S.25**.

Tables S.20-S.25 show atomic force comparisons of the AMBER and intraZIF FFs to PBE-D3(BJ) for the six atom types in SALEM-2. The intraZIF-FF more accurately represents atomic forces on the Zn, N, C₁, and H₁ atom types while AMBER-FF more accurately represents forces on the C₂ and H₂ atom types. Using the intraZIF-FF, we find atomic force NRMSD values of approximately 50% or less for the different atom types. While this comparison of energies

and forces indicates that the intraZIF-FF more accurately represents kinetic flexibility of ZIFs than the AMBER-FF, this PBE-D3(BJ) reference data could also be used to fit more realistic force field parameters through force matching⁹¹. As a reference for exceptional atomic force NRMSD values, Wang et al. performed a fitting procedure for water that is capable of achieving an atomic force NRMSD of 26%, with the claim that atomic force NRMSDs are capable of reaching values as low as 10-15%.⁷⁸ This suggests that the intraZIF-FF can be improved even further but most likely with diminishing returns with the current functional form.

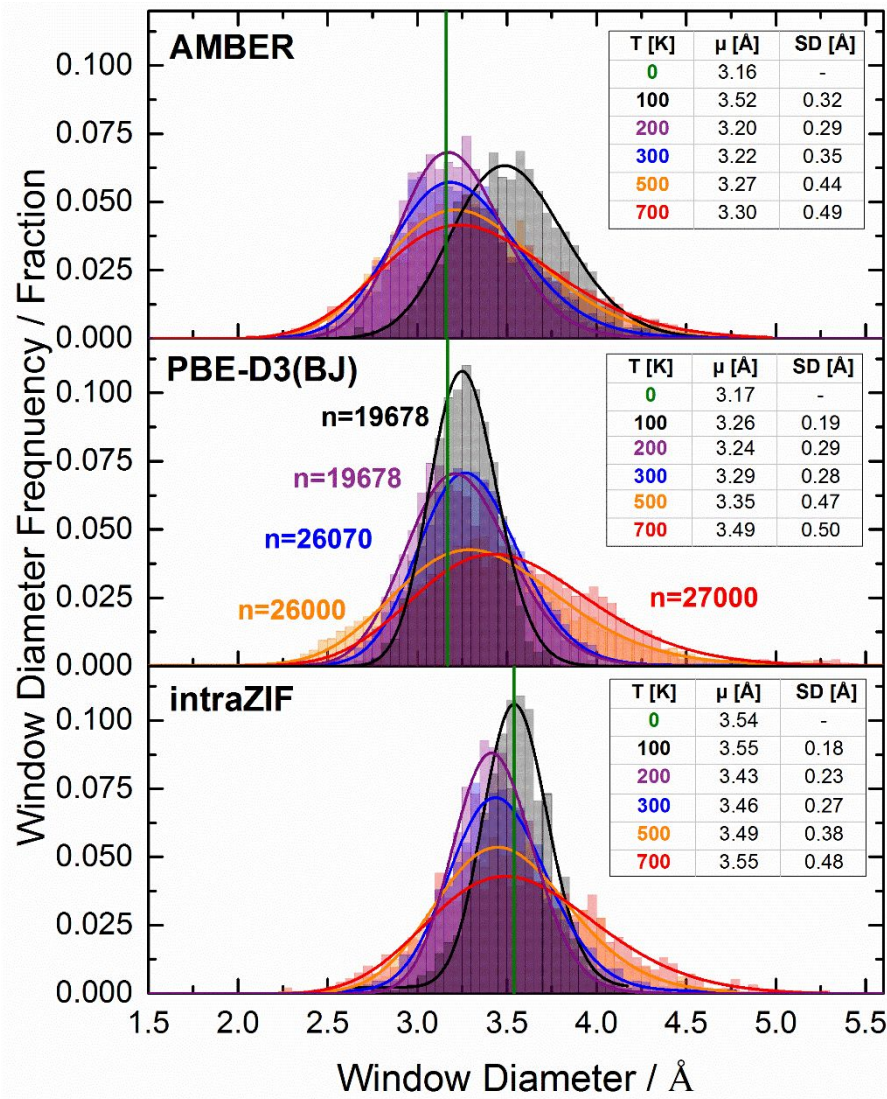


Figure 6. Window diameter histograms in SALEM-2 using PBE-D3(BJ) and the AMBER and intraZIF FFs at 0, 100, 200, 300, 500, and 700 K and 1.01 bar. Solid lines represent the lognormal distribution fits with the mean (μ) and standard deviation (SD) of these lognormal distributions reported in the table insets. There are 2000 samples for each histogram from the AMBER-FF and intraZIF-FF and the sample numbers for the histograms from PBE-D3(BJ) are reported in the center panel.

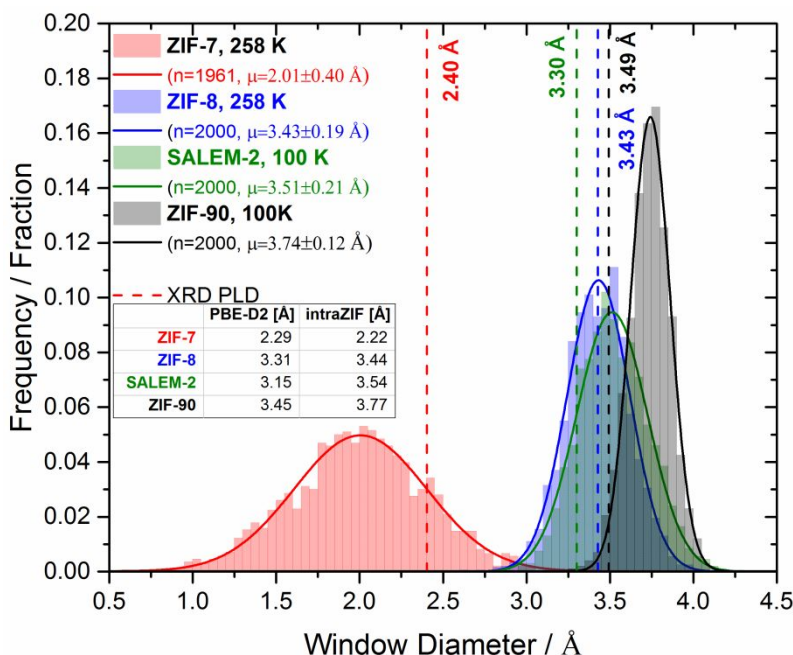


Figure 7. Window diameter histograms in SALEM-2, ZIF-7, ZIF-8, and ZIF-90 at 1.01 bar and temperatures at which the experimental crystal structures were resolved as predicted by the intraZIF-FF. The inset table compares the PLD (Å) of the energy minimized structures using PBE-D2 and the intraZIF-FF. Solid lines represent Gaussian distribution fits where the mean (μ) and standard deviation are reported in the legend.

3.4 Window Diameter Distributions

Examining the distribution of window diameters in small pore ZIFs can yield insights into the kinetic separation capabilities of these materials.^{20, 92} As our final independent test of the intraZIF-FF, we compared individual window diameter histograms measured from fully periodic BOMD simulations with NPT-MD simulations using both the AMBER and intraZIF FFs. The window diameters were calculated using a grid-based percolation method sampling only on individual window.¹⁹ **Figure 6** (middle panel) shows window diameter histograms for SALEM-2 simulated with BOMD at 100, 200, 300, 500, and 700 K and 1.0 bar from simulations with greater than 15 ps of production data with a 5 ps equilibration period. We also simulated the window diameter histograms with the AMBER (upper panel) and intraZIF (lower panel) FFs using conventional NPT-MD with snapshots taken every 0.5 ps over a 1000 ps trajectory.

Both FFs predict SALEM-2's large spread of window sizes (> 2 Å), which is significantly larger than the window diameter range observed in eight member ring (MR) zeolites⁹³ and ZIF-8 (~ 1 Å). The AMBER-FF more accurately reproduces the PBE-D3(BJ) pore limiting diameter at 0 K and the window diameter distributions at 200 - 500 K. At 700 K, the

intraZIF-FF more accurately reproduces the PBE-D3(BJ) window diameter distribution. Both FFs significantly overpredict the average window diameter at 100 K, but the intraZIF-FF predicts the correct standard deviation. While the AMBER-FF seems to better capture the window distributions of SALEM-2, we further examined the temperature dependence of the SALEM-2 unit cell volume (**Figure S21**) as it has a direct impact on the quality of window size and flexibility predictions. SALEM-2 exhibits a negative thermal expansion (NTE) from 200-500 K as predicted by PBE-D3(BJ) BOMD simulations ($\alpha_v = -68 \text{ MK}^{-1}$). This result is in disagreement with Bourg et al. who predicted, using isostress-isothermal MD simulations with a modified ZIF-8 FF, that SALEM-2 exhibited positive thermal expansion ($\alpha_v = +25 \text{ MK}^{-1}$) from 200-400 K.⁹⁴ The intraZIF and AMBER FFs both predict that SALEM-2 undergoes NTE over the 200-500 K temperature range with thermal expansion coefficients of -30 and -52 MK^{-1} respectively, but the intraZIF-FF more accurately predicts the unit cell volume than the AMBER-FF.

The results above provide evidence that the intraZIF-FF is useful for predicting structural properties of ZIFs. We therefore examined intraZIF-FF's ability to predict experimental PLDs. **Figure 7** shows the window diameter distributions of the 6MR for ZIF-8, ZIF-90, ZIF-7 and SALEM-2 at the same temperatures that single-crystal XRD refinements are available. The mean and standard deviation of the Gaussian distribution for ZIF-8 ($3.43 \pm 0.19 \text{ \AA}$) matches well with results from the AMBER-FF ($3.44 \pm 0.17 \text{ \AA}$) from our earlier work.¹⁹ We also include the PLDs from the PBE-D2 and intraZIF-FF energy minimized structures for reference. An interesting outlier in these comparisons in the inset table of **Figure 7** is ZIF-90. The intraZIF-FF predicts a slightly larger PLD (3.77 \AA) than the PLD predicted using PBE-D2 (3.45 \AA) of ZIF-90. Inspection of the energy minimized structure from the intraZIF-FF shows that the imidazolate linkers lie $\sim 18^\circ$ outside the plane approximately formed by the six Zn atoms. We defined this "swing angle" as the $\text{C}_2\text{-Zn}_1\text{-Zn}_2\text{-Zn}_3$ dihedral angle, which is similar to the dihedral angle defined by Coudert for analyzing the mIm swinging motion in ZIF-8⁹⁵. The imidazolate linkers in the ZIF-90 experimental and PBE-D2 structures are $\sim 4^\circ$ and $\sim 6^\circ$ outside the 6MR window plane. The slight tilting of the linkers causes this increase in the intraZIF-FF PLD.

The experimental PLDs rank as ZIF-7 (2.40 \AA) < SALEM-2 (3.30 \AA) < ZIF-8 (3.43 \AA) < ZIF-90 (3.49 \AA). This data suggests that diffusion in SALEM-2 would be slower in relation to the ZIF-8 and ZIF-90 structures. However, Karagiari et al. previously soaked ZIF-8 and SALEM-2 crystals in liquid n-hexane, cyclohexane, and toluene for 24 h at 25°C and upon

performing TGA-MS, determined that SALEM-2 crystals, unlike ZIF-8, adsorbed appreciable amounts of both cyclohexane or toluene.⁵⁹ The SALEM-2 distribution measured at 300 K (**Figure 6**) accesses window sizes up to 4.5 Å whereas the ZIF-8 window distribution measured at 258 K only accesses window diameters up to 4.0 Å. These distributions suggest that larger molecules may diffuse more easily in SALEM-2 than ZIF-8. This implication is explored further when we directly predict the diffusion properties of molecules in these ZIFs in **Section 4**.

Overall, **Figure 3a** indicates that intraZIF improved window size prediction for a set of 27 Im and 25 mIm polymorphs compared to the PBE-D2 reference. The transferability of our force field was a top priority in our fitting strategy. Because of the differences in equilibrium dihedral angle between the polymorphs used in our training set, it is impossible to accurately predict pore sizes of these 50 structures with high accuracy using one mathematical function. Nevertheless, **Figure 8** show a good agreement between our self-diffusion coefficients using intraZIF and experiments for 14 adsorbates.

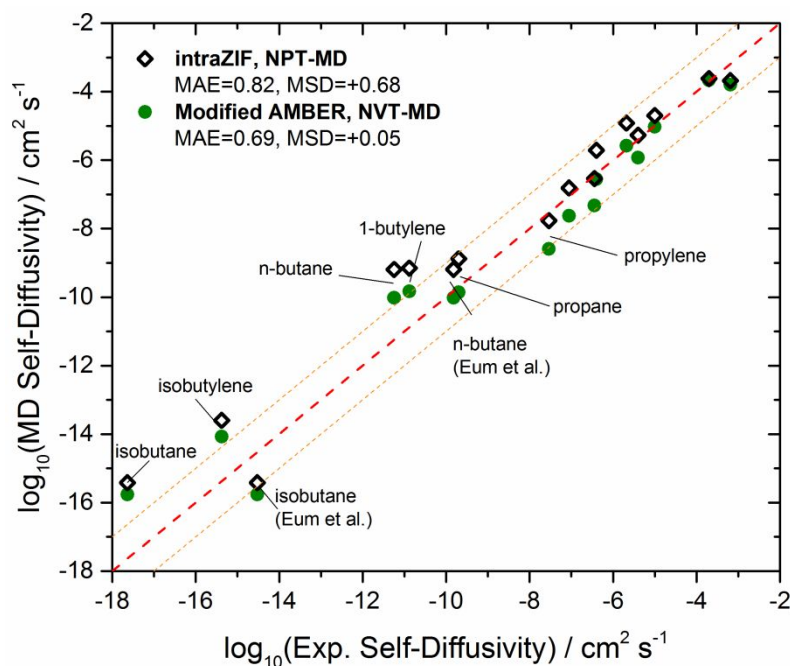


Figure 8. Self-diffusivities of 14 adsorbates as predicted by the modified AMBER-FF using NVT-MD from Verploegh et al.¹⁹ and the intraZIF-FF using NPT-MD (1.01 bar) in comparison to reference experimental diffusivities from Zhang et al.¹⁴ (unmarked) and Eum et al.⁹⁶ (marked) at 308 K. The dashed orange lines represent the order-of-magnitude accuracy expected from macroscopic uptake methods.

3.5 Screening of Thirty Adsorbates in SALEM-2, ZIF-8, and ZIF-90

The most rigorous test of the intraZIF force field is to determine its ability to accurately predict diffusion coefficients of adsorbates in different ZIF materials. We do this by comparing to prior simulated diffusion data that used the standard AMBER force field as well as to extant experimental diffusion coefficients. We further extend this study to adsorbates for which diffusion coefficients have not been experimentally measured. To our knowledge, this is the most comprehensive study of adsorbate diffusion in ZIFs having the SOD topology with simulations that include framework flexibility. **Figure 8** compares the predictions using the intraZIF-FF's with calculations using AMBER-FF's relative to experimental data. The MAE for the intraZIF-FF and the AMBER-FF are 0.82 and 0.69 (log base 10 scale) respectively, with the intraZIF-FF predicting slightly faster self-diffusion. The uncertainty in self-diffusion coefficients from experimental macroscopic uptake methods is typically at best an order of magnitude.⁹⁷ This is particularly apparent when comparing the results in **Figure 8** from independent experiments by Eum et al. and Zhang et al. for n-butane and isobutane diffusion in ZIF-8. Given this level of experimental uncertainty, it is reasonable to conclude that both sets of FF-based results in **Figure 8** show good agreement with experimentally observed diffusivities in ZIF-8.

Figure 9 shows the self-diffusivities at infinite dilution of all thirty adsorbates in SALEM-2, ZIF-90, and ZIF-8 at 308.15 K. All the predicted diffusion coefficients are reported in **Table S29**. For reference, we have plotted the PLDs from intraZIF-FF energy minimized structures as dashed lines. Consistent with previous studies⁹⁸⁻⁹⁹, adsorbates with molecular diameters much larger than the PLDs can diffuse readily. A key observation from the data in **Figure 9** is that SALEM-2 shows the fastest self-diffusivities for large molecules. This is supported by the window distributions of SALEM-2 and ZIF-90 in **Figure 7**. SALEM-2, while having an average window diameter 0.23 Å less than the average window diameter of ZIF-90, is able to access the same range of window diameters as ZIF-90. Coudert found that the libration angle for SALEM-2 is 35° while for ZIF-8 it is 15°, with free energy barriers to rotation of 3.5 and 15 kJ mol⁻¹ respectively, at 77 K using BOMD simulations.⁹⁵ However, these observations about the linker rotation and subsequent window distributions do not explain why a molecule as large as caffeine (~7 Å) is predicted to diffuse twelve (eighteen) orders of magnitude faster in SALEM-2 than ZIF-90 (ZIF-8). Clearly, the interaction of the adsorbates in the window region

influences the predicted self-diffusivities in a way that cannot be predicted in a simplistic way from structural features of the empty material.

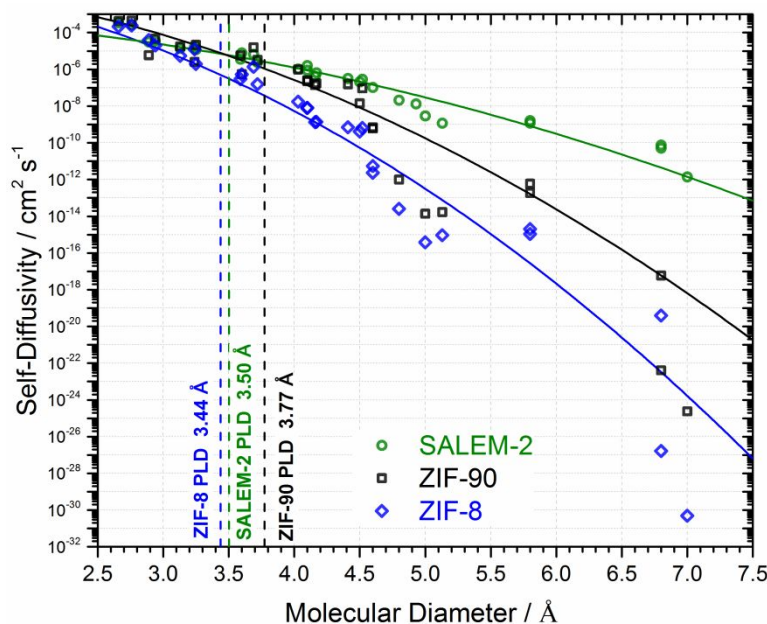


Figure 9. Self-diffusivities at infinite dilution of thirty adsorbates in SALEM-2, ZIF-8, and ZIF-90 with fits of **Equation 13** as solid lines. The intraZIF-FF predicted PLDs from energy-minimized structures are shown as dashed lines.

In our previous work, we made a thorough comparison of simulation results in ZIF-8 to experiments for C1-C4 hydrocarbons and light gases¹⁹. There are few experimental reports to which we can make direct comparisons to experiments for the larger adsorbates in **Figure 9**. These experiments utilize macroscopic uptake methods that measure transport diffusivities, which can be related to the corrected diffusivity using Darken's equation¹⁰⁰. Corrected diffusivities measured experimentally at infinite dilution can be directly compared to our predicted self-diffusivities, with the assumption that Maxwell-Stefan self-exchange diffusivities are large for cage-type ZIF materials. Zhang et al. reported corrected diffusivities in ZIF-8 for water, ethanol, 1-butanol, benzene, p-xylene, m-xylene, and o-xylene using vapor-phase kinetic uptake experiments at 50 °C.⁸² **Table S30** and **Figure S27** compare our simulated self-diffusivities to those measured by Zhang et al. Our predicted self-diffusivities follow the same ranking as those measured by Zhang et al.; however, most direct comparisons are different by several orders of magnitude. When measuring diffusion of large adsorbates using macroscopic uptake methods⁹⁷, external heat¹⁰¹ and mass transfer effects¹⁰² can have a large impact on the

accuracy of the reported diffusivities. Significant disagreement could also arise from significant surface barriers as Tanaka et al. reported observing for 1-butanol in ZIF-8 at 323 K.¹⁰³

Several of our predicted self-diffusivities of adsorbates with molecular diameters greater than 5.8 Å are worth examining in closer detail. Interestingly, we predicted that *p*-xylene diffuses twice as fast as benzene in ZIF-8, in disagreement with Zhang et al. To investigate this further, we calculated Gibbs free energy barriers of benzene and *p*-xylene at 275, 300, 325, 350, 375, and 400 K, finding a lower enthalpic barrier for *p*-xylene than benzene (**Figure S28**). This observation is similar to the work of Kolokathis et al. that determined *p*-xylene diffuses 100 times faster than benzene at low occupancies in silicalite-1 because it exhibits both a lower entropic and internal energy barrier.¹⁰⁴ We also predict extremely low diffusivities for *o*-xylene, *m*-xylene, and caffeine in ZIF-8 compared with the uptake experiments of Zhang et al. and Liédana et al.¹⁰⁵ Liédana et al. reported only caffeine uptake data at 80 °C so a caffeine transport diffusivity in ZIF-8 was estimated by fitting published data¹⁰⁵ to the analytical solution for diffusion into a sphere. For this calculation, average ZIF-8 particle radii were estimated at 125 nm from their reported characterization and were modeled as experiencing an instantaneous step change at the surface¹⁰⁶ with no caffeine depletion effects. The resulting transport diffusivity was approximately $1 \times 10^{-17} \text{ cm}^2 \text{ s}^{-1}$. We predicted a much slower self-diffusion coefficient for caffeine of $4.9 \times 10^{-31} \text{ cm}^2 \text{ s}^{-1}$ with a Gibbs free energy barrier of 150 kJ mol⁻¹ and transmission coefficient of 0.003. It is not clear what the source of this apparent discrepancy between our model and experiment is. It is possible that the intraZIF-FF is not appropriate for describing the very significant window distortions that must occur for a large molecule like caffeine to hop from cage to cage. It is also possible that defects could also exist in the ZIF-8 crystals used experimentally that enhance diffusion.¹⁰⁷

There have been fewer diffusion studies of ZIF-90, and we are aware of no experimental diffusion data in SALEM-2. Eum et al. reported experimental corrected diffusivities of *n*-butane, 1-butanol, and isobutane in ZIF-90 at 35 °C.⁹⁶ The diffusivities for these three molecules in ZIF-90 are one, two, and three orders of magnitude faster than the diffusivities in ZIF-8. We correctly predict the order of diffusivities as well as predicting that diffusion for these three adsorbates is faster in ZIF-90 than ZIF-8. It is interesting to note that the reported PLDs from the XRD-derived structures are nearly identical (ZIF-90: 3.5 Å, ZIF-8: 3.4 Å) yet minute differences in the window region can yield significantly faster diffusion. The

only computational study examining diffusion in ZIF-90 was performed by Chokbunpiam et al. who simulated H₂ and CH₄ self-diffusion using conventional NPT-MD (AMBER-FF) at low loading (2.5 molecules per cage) and 300 K. They reported self-diffusivities of 5.5×10^{-4} and 1.2×10^{-5} cm² s⁻¹ for H₂ and CH₄ respectively;¹⁰⁸ in excellent agreement, our simulated diffusivities for H₂ and CH₄ in ZIF-90 and 308 K are 4.54×10^{-4} and 2.14×10^{-5} cm² s⁻¹ respectively. These comparisons demonstrate that our simulations predict the trends seen experimentally and agree with similar studies by other computational groups.

It is interesting to consider whether there are simple scaling relationships that describe the large collection of diffusivities in **Figure 9**. An empirical relation between self-diffusivity and molecular diameter for penetrant diffusion in polymers was given in a seminal analysis of gas permeation in polymer membranes by Freeman:¹⁰⁹

$$\log(D_{s,i}) = -\left(\frac{1-a}{RT}\right)cd_i^2 + f\left(\frac{1-a}{RT}\right) - b \quad (12)$$

where the constants a , b , c , and d are independent of the adsorbate and depend only on the material in which the molecules are diffusing. By comparing this prediction to that of a reference adsorbate the following relationship is obtained:

$$\log\left(\frac{D_{s,i}}{D_{s,ref}}\right) = -c'(d_i^2 - d_{ref}^2) \quad (13)$$

where c' is dependent on temperature and the porous material but is independent of the adsorbate. Fits to this function using methane as the reference adsorbate are shown as solid lines in **Figure 9**. Our fit parameters c' are 0.415, 0.810, and 1.08 Å⁻² for SALEM-2, ZIF-90, and ZIF-8 respectively. These values are similar in magnitude with those of polymers, where Freeman reported that c' parameters at 308 K for polymers range between 0.15 Å⁻² for extremely flexible polydimethylsiloxane to 1.41 Å⁻² for a high-performance glassy polyimide. We note, however, that there is a plateau in the diffusivities for adsorbates with molecular diameters between 5 and 7 Å that is not captured by this scaling relationship. In the Supporting Information (**Figure S29**), we explored a separate metric from window distributions for quantifying ZIF flexibility and comment on its potential use in structure-property relationships for diffusion predictions.

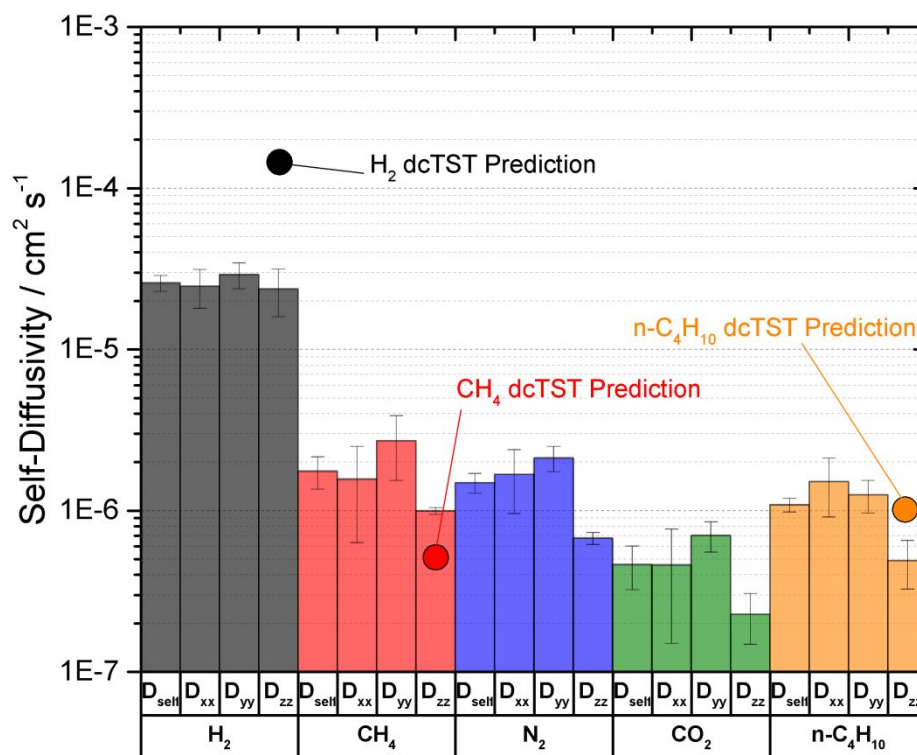


Figure 10. Self-diffusivities and the diagonal components of the diffusivity tensor from NPT-MD simulations at 308 K and a loading of three molecules per unit cell in ZIF-7. Overlaid on the plot are the dcTST diffusivity predictions for H₂, methane, and n-butane.

3.6 Diffusion in ZIF-7

Little is known about the transport of adsorbates through ZIF-7. ZIF-7 has a rhombohedral sodalite topology, unlike the cubic unit cells of ZIF-8 and ZIF-90. ZIF-7 was first synthesized by Yaghi and coworkers⁵⁷ and is not stable in liquid water¹¹⁰. Gascon and coworkers determined that the ZIF-7 unit cell expands through adsorption of CO₂ as well as C2 and C3 hydrocarbons at room temperature, revealing that these larger hydrocarbons can diffuse through the small windows (exp. PLD of 2.2 Å)¹³. ZIF-7 also exhibits a gate opening mechanism that allows for selective adsorption of C4 paraffins over olefins.¹² It also has been shown that solvents used in the synthesis can adsorb in the apparently inaccessible regions of ZIF-7 as seen from the templating solvents in the original reported crystal structure.⁵⁷ To complicate computational studies, ZIF-7 has three known stable phases depending on sample activation, as demonstrated by Zhao et al. (simulated XRD patterns in **Figure S30**).¹¹⁰ We chose to examine diffusion only in the ZIF-7-I phase for which we successfully performed a DFT energy minimization. We attempted a DFT energy minimization on the ZIF-7-II phase reported by Zhao et al. and were unable to obtain a converged structure. This further supports Du et al.

who noted that solving the structure of ZIF-7-II is challenging given its complexity and low symmetry.¹¹ As reported in **Figure 10**, self-diffusivity coefficients for H₂, methane, N₂, CO₂, and n-butane were measured with both dynamically corrected transition state theory (dcTST) and conventional NPT-MD simulations (refer to the Supporting Information for simulation details).

Several observations are apparent from the diffusivity data in **Figure 10**. First, our approach to predict diffusion using dcTST does not yield the same self-diffusivities as predicted by conventional NPT-MD. We originally chose a simple 1-D reaction coordinate for the dcTST simulations based on the PLD and H₂ diffusion (MSDs reported in **Figure S32b**) in the rigid ZIF-7-I phase as well as qualitative visualizations of the empty ZIF-7-I phase from fully flexible NPT-MD simulations. However, having examined MD trajectories of H₂ and CO₂ diffusion (**Figures S.34 and S.35**) in the flexible ZIF-7-I phase, we determined that adsorbates did not diffuse strictly along this chosen reaction coordinate. Clearly, applying dcTST to ZIF-7 requires a more complicated representation of adsorbate hopping than is available with the methods we used for ZIF-8, ZIF-90, and SALEM-2. Our second observation is that of the surprising kinetic flexibility of the ZIF-7-I phase, apparent from both the liquid-like diffusion coefficients of both methane and n-butane as well as the large standard deviation ($\sigma = 0.4 \text{ \AA}$) of the ZIF-7-I window diameter histogram reported in **Figure 7**. These results run counter to the notion that the ZIF-7-I phase, having a small PLD, is restricted to sieving small molecules such as H₂, CO₂, N₂, and CH₄. Lastly, we note that diffusion of n-butane is only slightly slower than the diffusion of methane. In **Figure S36**, we examined the influence of the finite loading on the accessible ZIF-7-I volume fraction and observe that n-butane significantly increases the accessible volume fraction as compared to methane. These results suggest that the flexibility of ZIF-7-I is highly coupled with adsorbate loading, yielding a larger than expected n-butane diffusivity.

To examine whether we predict reasonable diffusion trends in ZIF-7 with conventional MD, we compare to available computational and experimental literature regarding transport in ZIF-7. Using fully flexible MD simulations, Pilvar et al.¹¹¹ predicted a self-diffusion coefficient for H₂ in the ZIF-7-I phase of $2.7 \times 10^{-5} \text{ cm}^2 \text{ s}^{-1}$, in excellent agreement with our MD predicted self-diffusivity of 2.6×10^{-5} . They did not report the mechanism of H₂ diffusion or through which windows it was observed to diffuse. Wu et al. examined the adsorption kinetics of CO₂ and CH₄ in the ZIF-7-I at 298 K and predicted CH₄ diffuses more quickly than CO₂, in agreement with our NPT-MD self-diffusivities.¹¹² Rashidi et al. reported experimental transport diffusivities of

(3 ± 1) $\times 10^{-15}$ and (4 ± 1) $\times 10^{-16}$ cm² s⁻¹ respectively for n-butane and isobutane at 308 K in the ZIF-7-II phase.¹¹³ A direct comparison cannot be made to our results for the ZIF-7-I phase, but it is interesting that the diffusivity of n-butane is many orders of magnitude slower in the ZIF-7-II phase according to experimental measurements than the diffusivity of n-butane in the ZIF-7-I phase according to NPT-MD simulations. Du et al. reported that ZIF-7-II is a relatively dense phase that could experience more restricted flexibility and smaller PLDs than the ZIF-7-I phase¹¹, leading to these extremely low transport diffusivities. It is also possible that significant surface barrier resistances exist for ZIF-7 crystals.¹¹⁴ More comprehensive investigations of adsorbate diffusion through the various ZIF-7 phases are warranted, preferably using a combination of pulsed field gradient (PFG) NMR and molecular dynamics.

4. CONCLUSIONS

This study provides the basis for diffusion screening studies in flexible MOF materials with emphasis on the thoroughly studied ZIF family. To provide a consistent way of modeling ZIF flexibility rather than empirically tuning generic force fields to fit finite sets of experimental structural, adsorption, or diffusion data, we have developed the intraZIF force field using DFT reference calculations as fitting and test data. We demonstrated that the intraZIF-FF provides better prediction of various geometric and energetic properties than the AMBER-FF. The intraZIF-FF also more accurately reproduces kinetic flexibility through comparison of relative energies and atomic forces from BOMD simulations. Our piece-wise force field fitting process can be used to easily to develop extensions of the intraZIF-FF, enabling modeling of ZIFs with different imidazolate functionalities. The intraZIF force field can also be used to model adsorbate diffusion in mixed-linker ZIFs.¹¹⁵ The intraZIF-FF was used to produce the largest quantitative screening of diffusion in ZIFs, and essentially all MOFs, to date by including framework flexibility. Our predicted diffusion coefficients access a range of twenty-four orders of magnitude, a range made possible only using biased molecular dynamics sampling methods.

There have been many quantitative screening studies examining adsorption in MOFs^{31, 116} but it is difficult to perform this type of accurate screening to determine MOFs with molecular sieving potential. While it is increasingly possible to access superb computational capabilities, analytical models will need to be developed that merge empty framework flexibility characteristics with specific adsorbate-adsorbent interactions at transition states encountered

along the diffusion pathway. A motivating study performed by Witman et al. develops a simple analytical model to predict the influence of pore size distributions on Henry's constants.¹¹⁷ In a similar fashion, the intraZIF-FF could be used to develop structure-property relationships between diffusivities and flexibility observables (e.g. linker swing angles, window size distributions, etc.) possibly using hypothetical ZIF polymorphs, a list that easily extends to well over a million structures based on zeolite analogues¹¹⁸. Our study provides a possible basis for predicting diffusion quantitatively in ZIFs with a range of topologies and imidazolate functionalities, by providing a representative force field, proving the ability of this force field, and predicting the diffusivities of thirty small molecules.

5. ASSOCIATED CONTENT

Supporting information

Included are the intraZIF and AMBER bonded and nonbonded force field parameters for imidazolate, methyl-2-imidazolate, carboxaldehyde-2-imidazolate, and benzimidazolate ZIFs. Specific details of fitting the N-Zn Morse potential as well as a refitting of the N-Zn-N and N-Zn-C stretches are also included. Geometric characteristics of the SALEM-2, ZIF-7, ZIF-8, and ZIF-90 energy minimized structures are included for PBE-D2, PBE-D3(BJ), the AMBER-FF, and the intraZIF-FF. Geometric and thermodynamic stability predictions are given for the Im and mIm polymorphs as well as analysis of the BOMD trajectories. Information regarding light gas diffusion in SALEM-2, ZIF-8, ZIF-90, and ZIF-7: adsorbate force fields, molecular diameters, free energy barriers, dynamical corrections to TST rates, self-diffusion coefficients, comparisons to experimental diffusivities, the fitting procedure for the empirical relationship between molecular diameter and self-diffusivity, definition of linker swinging observables, and a brief description of diffusion in ZIF-7. CP2K input files are also included for performing energy minimization as well as BOMD simulations.

6. AUTHOR INFORMATION

Corresponding Author

*david.sholl@chbe.gatech.edu

Notes

These authors declare no competing financial interest.

7. ACKNOWLEDGEMENTS

RJV, JCH and DSS received support from the National Science Foundation grant number 1604375. DT and DSS received support from the Department of Energy Nanoporous Materials Genome Center, supported by the U.S. Department of Energy, Office of Basic Energy Sciences,

Division of Chemical Sciences, Geosciences and Biosciences under Award DEFG02-12ER16362. We thank Brian Pimentel for helpful discussions on interpreting experimental diffusion data taken using kinetic uptake experiments.

8. REFERENCES

1. Furukawa, H.; Cordova, K. E.; O’Keeffe, M.; Yaghi, O. M., The Chemistry and Applications of Metal-Organic Frameworks. *Science* **2013**, *341*, 12304441-12304442.
2. Peng, Y.; Li, Y.; Ban, Y.; Jin, H.; Jiao, W.; Liu, X.; Yang, W., Metal-Organic Framework Nanosheets as Building Blocks for Molecular Sieving Membranes. *Science* **2014**, *346*, 1356-1359.
3. Corma, A.; García, H.; Llabrés i Xamena, F. X., Engineering Metal Organic Frameworks for Heterogeneous Catalysis. *Chemical Reviews* **2010**, *110*, 4606-4655.
4. Van de Voorde, B.; Bueken, B.; Denayer, J.; De Vos, D., Adsorptive Separation on Metal-Organic Frameworks in the Liquid Phase. *Chemical Society Reviews* **2014**, *43*, 5766-5788.
5. Li, B.; Wen, H.-M.; Zhou, W.; Chen, B., Porous Metal–Organic Frameworks for Gas Storage and Separation: What, How, and Why? *The Journal of Physical Chemistry Letters* **2014**, *5*, 3468-3479.
6. Stavila, V.; Talin, A. A.; Allendorf, M. D., Mof-Based Electronic and Opto-Electronic Devices. *Chemical Society Reviews* **2014**, *43*, 5994-6010.
7. Kreno, L. E.; Leong, K.; Farha, O. K.; Allendorf, M.; Van Duyne, R. P.; Hupp, J. T., Metal-Organic Framework Materials as Chemical Sensors. *Chemical Reviews* **2012**, *112*, 1105-1125.
8. Coudert, F. X.; Boutin, A.; Jeffroy, M.; Mellot-Draznieks, C.; Fuchs, A. H., Thermodynamic Methods and Models to Study Flexible Metal-Organic Frameworks. *Chemphyschem : a European journal of chemical physics and physical chemistry* **2011**, *12*, 247-258.
9. Pimentel, B. R.; Parulkar, A.; Zhou, E.-k.; Brunelli, N. A.; Lively, R. P., Zeolitic Imidazolate Frameworks: Next-Generation Materials for Energy-Efficient Gas Separations. *ChemSusChem* **2014**, *7*, 3202-3240.
10. Wharmby, M. T., et al., Extreme Flexibility in a Zeolitic Imidazolate Framework: Porous to Dense Phase Transition in Desolvated ZIF-4. *Angewandte Chemie* **2015**, *127*, 6547-6551.
11. Du, Y.; Wooller, B.; Nines, M.; Kortunov, P.; Paur, C. S.; Zengel, J.; Weston, S. C.; Ravikovitch, P. I., New High- and Low-Temperature Phase Changes of ZIF-7: Elucidation and Prediction of the Thermodynamics of Transitions. *Journal of the American Chemical Society* **2015**, *137*, 13603-13611.
12. van den Bergh, J.; Gucuyener, C.; Pidko, E. A.; Hensen, E. J.; Gascon, J.; Kapteijn, F., Understanding the Anomalous Alkane Selectivity of ZIF-7 in the Separation of Light Alkane/Alkene Mixtures. *Chemistry* **2011**, *17*, 8832-40.
13. Gucuyener, C.; van den Bergh, J.; Gascon, J.; Kapteijn, F., Ethane/Ethene Separation Turned on Its Head: Selective Ethane Adsorption on the Metal-Organic Framework ZIF-7 through a Gate-Opening Mechanism. *Journal of the American Chemical Society* **2010**, *132*, 17704-17706.
14. Zhang, C.; Lively, R. P.; Zhang, K.; Johnson, J. R.; Karvan, O.; Koros, W. J., Unexpected Molecular Sieving Properties of Zeolitic Imidazolate Framework-8. *The Journal of Physical Chemistry Letters* **2012**, *3*, 2130-2134.
15. Thompson, J. A.; Blad, C. R.; Brunelli, N. A.; Lydon, M. E.; Lively, R. P.; Jones, C. W.; Nair, S., Hybrid Zeolitic Imidazolate Frameworks: Controlling Framework Porosity and Functionality by Mixed-Linker Synthesis. *Chemistry of Materials* **2012**, *24*, 1930-1936.
16. Brown, A. J.; Brunelli, N. A.; Eum, K.; Rashidi, F.; Johnson, J. R.; Koros, W. J.; Jones, C. W.; Nair, S., Separation Membranes. Interfacial Microfluidic Processing of Metal-Organic Framework Hollow Fiber Membranes. *Science* **2014**, *345*, 72-75.
17. Pimentel, B. R.; Lively, R. P., Enabling Kinetic Light Hydrocarbon Separation Via Crystal Size Engineering of ZIF-8. *Industrial & Engineering Chemistry Research* **2016**, *55*, 12467-12476.
18. Sholl, D. S.; Lively, R. P., Seven Chemical Separations to Change the World. *Nature* **2016**, *532*, 435-437.

19. Verploegh, R. J.; Nair, S.; Sholl, D. S., Temperature and Loading-Dependent Diffusion of Light Hydrocarbons in ZIF-8 as Predicted through Fully Flexible Molecular Simulations. *Journal of the American Chemical Society* **2015**, *137*, 15760-15771.
20. Haldoupis, E.; Nair, S.; Sholl, D. S., Pore Size Analysis of >250 000 Hypothetical Zeolites. *Physical Chemistry Chemical Physics* **2011**, *13*, 5053-5060.
21. Haldoupis, E.; Nair, S.; Sholl, D. S., Efficient Calculation of Diffusion Limitations in Metal Organic Framework Materials: A Tool for Identifying Materials for Kinetic Separations. *Journal of the American Chemical Society* **2010**, *132*, 7528-7539.
22. Smit, B.; Maesen, T. L. M., Molecular Simulations of Zeolites: Adsorption, Diffusion, and Shape Selectivity. *Chemical Reviews* **2008**, *108*, 4125-4184.
23. Demontis, P.; Suffritti, G. B., A Comment on the Flexibility of Framework in Molecular Dynamics Simulations of Zeolites. *Microporous and Mesoporous Materials* **2009**, *125*, 160-168.
24. Greathouse, J. A.; Allendorf, M. D., The Interaction of Water with Mof-5 Simulated by Molecular Dynamics. *Journal of the American Chemical Society* **2006**, *128*, 10678-10679.
25. Greathouse, J. A.; Allendorf, M. D., Force Field Validation for Molecular Dynamics Simulations of Irmof-1 and Other Isorecticular Zinc Carboxylate Coordination Polymers. *Journal of Physical Chemistry C* **2008**, *112*, 5795-5802.
26. Dubbeldam, D.; Walton, K. S.; Ellis, D. E.; Snurr, R. Q., Exceptional Negative Thermal Expansion in Isorecticular Metal–Organic Frameworks. *Angewandte Chemie* **2007**, *119*, 4580-4583.
27. Salles, F.; Ghoufi, A.; Maurin, G.; Bell, R. G.; Mellot-Draznieks, C.; Ferey, G., Molecular Dynamics Simulations of Breathing Mofs: Structural Transformations of Mil-53(Cr) Upon Thermal Activation and CO₂ Adsorption. *Angewandte Chemie-International Edition* **2008**, *47*, 8487-8491.
28. Gee, J. A.; Sholl, D. S., Effect of Framework Flexibility on C₈ Aromatic Adsorption at High Loadings in Metal–Organic Frameworks. *The Journal of Physical Chemistry C* **2015**, *120*, 370-376.
29. Li, P.; Merz, K. M., Mcpb.Py: A Python Based Metal Center Parameter Builder. *Journal of Chemical Information and Modeling* **2016**, *56*, 599-604.
30. Couprie, D. E.; Addicoat, M. A.; Heine, T., Extension of the Universal Force Field for Metal–Organic Frameworks. *Journal of Chemical Theory and Computation* **2016**, *12*, 5215-5225.
31. Chung, Y. G.; Camp, J.; Haranczyk, M.; Sikora, B. J.; Bury, W.; Krungleviciute, V.; Yildirim, T.; Farha, O. K.; Sholl, D. S.; Snurr, R. Q., Computation-Ready, Experimental Metal–Organic Frameworks: A Tool to Enable High-Throughput Screening of Nanoporous Crystals. *Chemistry of Materials* **2014**, *26*, 6185-6192.
32. Seminario, J. M., Calculation of Intramolecular Force Fields from Second-Derivative Tensors. *International Journal of Quantum Chemistry* **1996**, *30*, 1271-1277.
33. Hagler, A. T., Quantum Derivative Fitting and Biomolecular Force Fields: Functional Form, Coupling Terms, Charge Flux, Nonbond Anharmonicity, and Individual Dihedral Potentials. *Journal of Chemical Theory and Computation* **2015**, *11*, 5555-5572.
34. Wang, L.-P.; Martinez, T. J.; Pande, V. S., Building Force Fields: An Automatic, Systematic, and Reproducible Approach. *The journal of physical chemistry letters* **2014**, *5*, 1885-1891.
35. Tafipolsky, M.; Amirjalayer, S.; Schmid, R., Ab Initio Parametrized Mm3 Force Field for the Metal–Organic Framework Mof-5. *Journal of Computational Chemistry* **2007**, *28*, 1169-1176.
36. Amirjalayer, S.; Tafipolsky, M.; Schmid, R., Molecular Dynamics Simulation of Benzene Diffusion in Mof-5: Importance of Lattice Dynamics. *Angewandte Chemie International Edition* **2007**, *46*, 463-466.
37. Bureekaew, S.; Amirjalayer, S.; Tafipolsky, M.; Spickermann, C.; Roy, T. K.; Schmid, R., Mof-Ff - a Flexible First-Principles Derived Force Field for Metal–Organic Frameworks. *Phys. Status Solidi B* **2013**, *250*, 1128-1141.
38. Allinger, N. L.; Yuh, Y. H.; Lii, J. H., Molecular Mechanics. The Mm3 Force Field for Hydrocarbons. 1. *Journal of the American Chemical Society* **1989**, *111*, 8551-8566.
39. Bristow, J. K.; Tiana, D.; Walsh, A., Transferable Force Field for Metal–Organic Frameworks from First-Principles: Btw-Ff. *Journal of Chemical Theory and Computation* **2014**, *10*, 4644-4652.

40. Vanduyfhuys, L.; Vandenbrande, S.; Verstraelen, T.; Schmid, R.; Waroquier, M.; Van Speybroeck, V., Quickff: A Program for a Quick and Easy Derivation of Force Fields for Metal-Organic Frameworks from Ab Initio Input. *Journal of Computational Chemistry* **2015**, *36*, 1015-1027.
41. Rogge, S. M. J.; Wieme, J.; Vanduyfhuys, L.; Vandenbrande, S.; Maurin, G.; Verstraelen, T.; Waroquier, M.; Van Speybroeck, V., Thermodynamic Insight in the High-Pressure Behavior of UiO-66: Effect of Linker Defects and Linker Expansion. *Chemistry of Materials* **2016**, *28*, 5721-5732.
42. Hertäg, L.; Bux, H.; Caro, J.; Chmelik, C.; Remsungnen, T.; Knauth, M.; Fritzsche, S., Diffusion of CH₄ and H₂ in ZIF-8. *Journal of Membrane Science* **2011**, *377*, 36-41.
43. Battisti, A.; Taioli, S.; Garberoglio, G., Zeolitic Imidazolate Frameworks for Separation of Binary Mixtures of CO₂, CH₄, N₂ and H₂: A Computer Simulation Investigation. *Microporous and Mesoporous Materials* **2011**, *143*, 46-53.
44. Thornton, A. W.; Dubbeldam, D.; Liu, M. S.; Ladewig, B. P.; Hill, A. J.; Hill, M. R., Feasibility of Zeolitic Imidazolate Framework Membranes for Clean Energy Applications. *Energy & Environmental Science* **2012**, *5*, 7637-7646.
45. Zheng, B.; Sant, M.; Demontis, P.; Suffritti, G. B., Force Field for Molecular Dynamics Computations in Flexible ZIF-8 Framework. *The Journal of Physical Chemistry C* **2012**, *116*, 933-938.
46. Gee, J. A.; Chung, J.; Nair, S.; Sholl, D. S., Adsorption and Diffusion of Small Alcohols in Zeolitic Imidazolate Frameworks ZIF-8 and ZIF-90. *Journal of Physical Chemistry C* **2013**, *117*, 3169-3176.
47. Zhang, L.; Hu, Z.; Jiang, J., Sorption-Induced Structural Transition of Zeolitic Imidazolate Framework-8: A Hybrid Molecular Simulation Study. *Journal of the American Chemical Society* **2013**, *135*, 3722-3728.
48. Chokbunpiam, T.; Chanajaree, R.; Saengsawang, O.; Reimann, S.; Chmelik, C.; Fritzsche, S.; Caro, J.; Remsungnen, T.; Hannongbua, S., The Importance of Lattice Flexibility for the Migration of Ethane in ZIF-8: Molecular Dynamics Simulations. *Microporous and Mesoporous Materials* **2013**, *174*, 126-134.
49. Krokidas, P.; Castier, M.; Moncho, S.; Sredojevic, D. N.; Brothers, E. N.; Kwon, H. T.; Jeong, H.-K.; Lee, J. S.; Economou, I. G., ZIF-67 Framework: A Promising New Candidate for Propylene/Propane Separation. Experimental Data and Molecular Simulations. *The Journal of Physical Chemistry C* **2016**, *120*, 8116-8124.
50. Phuong, V. T.; Chokbunpiam, T.; Fritzsche, S.; Remsungnen, T.; Rungrotmongkol, T.; Chmelik, C.; Caro, J.; Hannongbua, S., Methane in Zeolitic Imidazolate Framework ZIF-90: Adsorption and Diffusion by Molecular Dynamics and Gibbs Ensemble Monte Carlo. *Microporous and Mesoporous Materials* **2016**, *235*, 69-77.
51. Gao, M.; Misquitta, A. J.; H. N. Rimmer, L.; Dove, M. T., Molecular Dynamics Simulation Study of Various Zeolitic Imidazolate Framework Structures. *Dalton Transactions* **2016**, *45*, 4289-4302.
52. Wu, R.; Lu, Z.; Cao, Z.; Zhang, Y., A Transferable Nonbonded Pairwise Force Field to Model Zinc Interactions in Metalloproteins. *Journal of Chemical Theory and Computation* **2011**, *7*, 433-443.
53. Hoops, S. C.; Anderson, K. W.; Merz, K. M., Force Field Design for Metalloproteins. *Journal of the American Chemical Society* **1991**, *113*, 8262-8270.
54. Peters, M. B.; Yang, Y.; Wang, B.; Füsti-Molnár, L. s.; Weaver, M. N.; Merz Jr, K. M., Structural Survey of Zinc-Containing Proteins and Development of the Zinc Amber Force Field (Zaff). *Journal of chemical theory and computation* **2010**, *6*, 2935-2947.
55. Sakharov, D. V.; Lim, C., Force Fields Including Charge Transfer and Local Polarization Effects: Application to Proteins Containing Multi/Heavy Metal Ions. *Journal of Computational Chemistry* **2009**, *30*, 191-202.
56. Groom, C. R.; Bruno, I. J.; Lightfoot, M. P.; Ward, S. C., The Cambridge Structural Database. *Acta Crystallographica Section B: Structural Science, Crystal Engineering and Materials* **2016**, *72*, 171-179.

57. Park, K. S.; Ni, Z.; Côté, A. P.; Choi, J. Y.; Huang, R.; Uribe-Romo, F. J.; Chae, H. K.; O’Keeffe, M.; Yaghi, O. M., Exceptional Chemical and Thermal Stability of Zeolitic Imidazolate Frameworks. *Proceedings of the National Academy of Sciences* **2006**, *103*, 10186-10191.
58. Morris, W.; Doonan, C. J.; Furukawa, H.; Banerjee, R.; Yaghi, O. M., Crystals as Molecules: Postsynthesis Covalent Functionalization of Zeolitic Imidazolate Frameworks. *Journal of the American Chemical Society* **2008**, *130*, 12626-12627.
59. Karagiari, O.; Lalonde, M. B.; Bury, W.; Sarjeant, A. A.; Farha, O. K.; Hupp, J. T., Opening ZIF-8: A Catalytically Active Zeolitic Imidazolate Framework of Sodalite Topology with Unsubstituted Linkers. *Journal of the American Chemical Society* **2012**, *134*, 18790-18796.
60. Kresse, G.; Furthmüller, J., Efficient Iterative Schemes for Ab Initio Total-Energy Calculations Using a Plane-Wave Basis Set. *Physical Review B* **1996**, *54*, 11169-11186.
61. Sholl, D. S.; Steckel, J. A., *Density Functional Theory: A Practical Introduction*; John Wiley & Sons, Inc.: Hoboken, NJ, 2009.
62. Perdew, J. P.; Burke, K.; Ernzerhof, M., Generalized Gradient Approximation Made Simple. *Physical Review Letters* **1996**, *77*, 3865-3868.
63. Grimme, S., Semiempirical Gga-Type Density Functional Constructed with a Long-Range Dispersion Correction. *Journal of computational chemistry* **2006**, *27*, 1787-1799.
64. Grimme, S.; Ehrlich, S.; Goerigk, L., Effect of the Damping Function in Dispersion Corrected Density Functional Theory. *Journal of Computational Chemistry* **2011**, *32*, 1456-1465.
65. Grimme, S.; Antony, J.; Ehrlich, S.; Krieg, H., A Consistent and Accurate Ab Initio Parametrization of Density Functional Dispersion Correction (Dft-D) for the 94 Elements H-Pu. *The Journal of Chemical Physics* **2010**, *132*, 154104.
66. Krokidas, P.; Moncho, S.; Brothers, E. N.; Castier, M.; Jeong, H. K.; Economou, I. G., On the Efficient Separation of Gas Mixtures with the Mixed-Linker Zeolitic-Imidazolate Framework-7-8. *ACS Applied Materials & Interfaces* **2018**, *10*, 39631-39644.
67. Manz, T. A.; Sholl, D. S., Chemically Meaningful Atomic Charges That Reproduce the Electrostatic Potential in Periodic and Nonperiodic Materials. *Journal of Chemical Theory and Computation* **2010**, *6*, 2455-2468.
68. Manz, T. A.; Sholl, D. S., Improved Atoms-in-Molecule Charge Partitioning Functional for Simultaneously Reproducing the Electrostatic Potential and Chemical States in Periodic and Nonperiodic Materials. *Journal of Chemical Theory and Computation* **2012**, *8*, 2844-2867.
69. Hutter, J.; Iannuzzi, M.; Schiffmann, F.; VandeVondele, J., Cp2k: Atomistic Simulations of Condensed Matter Systems. *Wires Comput Mol Sci* **2014**, *4*, 15-25.
70. VandeVondele, J.; Krack, M.; Mohamed, F.; Parrinello, M.; Chassaing, T.; Hutter, J., Quickstep: Fast and Accurate Density Functional Calculations Using a Mixed Gaussian and Plane Waves Approach. *Comput Phys Commun* **2005**, *167*, 103-128.
71. VandeVondele, J.; Hutter, J., An Efficient Orbital Transformation Method for Electronic Structure Calculations. *J Chem Phys* **2003**, *118*, 4365-4369.
72. Krack, M.; Parrinello, M., All-Electron Ab-Initio Molecular Dynamics. *Physical Chemistry Chemical Physics* **2000**, *2*, 2105-2112.
73. Lippert, G.; Hutter, J.; Parrinello, M., The Gaussian and Augmented-Plane-Wave Density Functional Method for Ab Initio Molecular Dynamics Simulations. *Theor Chem Acc* **1999**, *103*, 124-140.
74. Goedecker, S.; Teter, M.; Hutter, J., Separable Dual-Space Gaussian Pseudopotentials. *Physical Review B* **1996**, *54*, 1703-1710.
75. Hartwigsen, C.; Goedecker, S.; Hutter, J., Relativistic Separable Dual-Space Gaussian Pseudopotentials from H to Rn. *Physical Review B* **1998**, *58*, 3641-3662.
76. Frenkel, D.; Smit, B., *Understanding Molecular Simulation: From Algorithms to Applications*, 2nd ed.; Academic Press: New York, 2002.
77. Plimpton, S., Fast Parallel Algorithms for Short-Range Molecular-Dynamics. *Journal of Computational Physics* **1995**, *117*, 1-19.

78. Wang, L.-P.; Head-Gordon, T.; Ponder, J. W.; Ren, P.; Chodera, J. D.; Eastman, P. K.; Martinez, T. J.; Pande, V. S., Systematic Improvement of a Classical Molecular Model of Water. *The Journal of Physical Chemistry B* **2013**, *117*, 9956-9972.
79. Guvench, O.; MacKerell, A. D., Automated Conformational Energy Fitting for Force-Field Development. *Journal of Molecular Modeling* **2008**, *14*, 667-679.
80. Allinger, N. L.; Zhou, X.; Bergsma, J., Molecular Mechanics Parameters. *Journal of Molecular Structure: THEOCHEM* **1994**, *312*, 69-83.
81. Grimme, S.; Steinmetz, M., Effects of London Dispersion Correction in Density Functional Theory on the Structures of Organic Molecules in the Gas Phase. *Physical Chemistry Chemical Physics* **2013**, *15*, 16031-16042.
82. Zhang, K.; Lively, R. P.; Zhang, C.; Chance, R. R.; Koros, W. J.; Sholl, D. S.; Nair, S., Exploring the Framework Hydrophobicity and Flexibility of ZIF-8: From Biofuel Recovery to Hydrocarbon Separations. *Journal of Physical Chemistry Letters* **2013**, *4*, 3618-3622.
83. June, R. L.; Bell, A. T.; Theodorou, D. N., Transition-State Studies of Xenon and Sf6 Diffusion in Silicalite. *Journal of Physical Chemistry* **1991**, *95*, 8866-8878.
84. Dubbeldam, D.; Beerdse, E.; Vlugt, T. J. H.; Smit, B., Molecular Simulation of Loading-Dependent Diffusion in Nanoporous Materials Using Extended Dynamically Corrected Transition State Theory. *J Chem Phys* **2005**, *122*, 224712.
85. Fiorin, G.; Klein, M. L.; Hénin, J., Using Collective Variables to Drive Molecular Dynamics Simulations. *Molecular Physics* **2013**, *111*, 3345-3362.
86. Grossfield, A., Wham: The Weighted Histogram Analysis Method, Version 2.0.9, <http://Membrane.Urnc.Rochester.Edu/Content/Wham>. Department of Biochemistry and Biophysics, University of Rochester Medical Center: Rochester, NY, 2013. (accessed Oct. 15, 2014).
87. Willems, T. F.; Rycroft, C. H.; Kazi, M.; Meza, J. C.; Haranczyk, M., Algorithms and Tools for High-Throughput Geometry-Based Analysis of Crystalline Porous Materials. *Microporous and Mesoporous Materials* **2012**, *149*, 134-141.
88. Baburin, I. A.; Leoni, S.; Seifert, G., Enumeration of Not-yet-Synthesized Zeolitic Zinc Imidazolate Mof Networks: A Topological and Dft Approach. *The Journal of Physical Chemistry B* **2008**, *112*, 9437-9443.
89. Baburin, I. A.; Leoni, S., The Energy Landscapes of Zeolitic Imidazolate Frameworks (ZIFs): Towards Quantifying the Presence of Substituents on the Imidazole Ring. *Journal of Materials Chemistry* **2012**, *22*, 10152-10154.
90. Chapman, K. W.; Halder, G. J.; Chupas, P. J., Pressure-Induced Amorphization and Porosity Modification in a Metal–Organic Framework. *Journal of the American Chemical Society* **2009**, *131*, 17546-17547.
91. Gabrieli, A.; Sant, M.; Demontis, P.; Suffritti, G. B., Fast and Efficient Optimization of Molecular Dynamics Force Fields for Microporous Materials: Bonded Interactions Via Force Matching. *Microporous and Mesoporous Materials* **2014**, *197*, 339-347.
92. Watanabe, T.; Sholl, D. S., Accelerating Applications of Metal-Organic Frameworks for Gas Adsorption and Separation by Computational Screening of Materials. *Langmuir : the ACS journal of surfaces and colloids* **2012**, *28*, 14114-28.
93. Boulfelfel, S. E.; Ravikovitch, P. I.; Koziol, L.; Sholl, D. S., Improved Hill–Sauer Force Field for Accurate Description of Pores in 8-Ring Zeolites. *The Journal of Physical Chemistry C* **2016**, *120*, 14140-14148.
94. Bourg, L. B. d.; Ortiz, A. U.; Boutin, A.; Coudert, F.-X., Thermal and Mechanical Stability of Zeolitic Imidazolate Frameworks Polymorphs. *APL Materials* **2014**, *2*, 124110.
95. Coudert, F.-X., Molecular Mechanism of Swing Effect in Zeolitic Imidazolate Framework ZIF-8: Continuous Deformation Upon Adsorption. *Chemphyschem : a European journal of chemical physics and physical chemistry* **2017**, *18*, 2732-2738.
96. Eum, K.; Jayachandrababu, K. C.; Rashidi, F.; Zhang, K.; Leisen, J.; Graham, S.; Lively, R. P.; Chance, R. R.; Sholl, D. S.; Jones, C. W., Highly Tunable Molecular Sieving and Adsorption Properties

- of Mixed-Linker Zeolitic Imidazolate Frameworks. *Journal of the American Chemical Society* **2015**, *137*, 4191–4197.
97. Kärger, J.; Valiullin, R., Mass Transfer in Mesoporous Materials: The Benefit of Microscopic Diffusion Measurement. *Chemical Society Reviews* **2013**, *42*, 4172–4197.
98. Haldoupis, E.; Watanabe, T.; Nair, S.; Sholl, D. S., Quantifying Large Effects of Framework Flexibility on Diffusion in Mofs: CH₄ and CO₂ in ZIF-8. *Chemphyschem : a European journal of chemical physics and physical chemistry* **2012**, *13*, 3449–3452.
99. Hu, Z.; Zhang, L.; Jiang, J., Development of a Force Field for Zeolitic Imidazolate Framework-8 with Structural Flexibility. *The Journal of Chemical Physics* **2012**, *136*, 244703.
100. Kärger, J.; Binder, T.; Chmelik, C.; Hibbe, F.; Krautscheid, H.; Krishna, R.; Weitkamp, J., Microimaging of Transient Guest Profiles to Monitor Mass Transfer in Nanoporous Materials. *Nature materials* **2014**, *13*, 333–343.
101. Lee, L.; Ruthven, D. M., Analysis of Thermal Effects in Adsorption Rate Measurements. *Journal of the Chemical Society, Faraday Transactions 1: Physical Chemistry in Condensed Phases* **1979**, *75*, 2406–2422.
102. Brandani, S., Analysis of the Piezometric Method for the Study of Diffusion in Microporous Solids: Isothermal Case. *Adsorption* **1998**, *4*, 17–24.
103. Tanaka, S.; Fujita, K.; Miyake, Y.; Miyamoto, M.; Hasegawa, Y.; Makino, T.; Van der Perre, S.; Cousin Saint Remi, J.; Van Assche, T.; Baron, G. V., Adsorption and Diffusion Phenomena in Crystal Size Engineered ZIF-8 Mof. *The Journal of Physical Chemistry C* **2015**, *119*, 28430–28439.
104. Kolokathis, P. D.; Káli, G.; Jobic, H.; Theodorou, D. N., Diffusion of Aromatics in Silicalite-1: Experimental and Theoretical Evidence of Entropic Barriers. *The Journal of Physical Chemistry C* **2016**, *120*, 21410–21426.
105. Liédana, N.; Galve, A.; Rubio, C.; Téllez, C.; Coronas, J., Caf@ZIF-8: One-Step Encapsulation of Caffeine in Mof. *ACS Applied Materials & Interfaces* **2012**, *4*, 5016–5021.
106. Crank, J., *The Mathematics of Diffusion*; Oxford University Press: New York, 1979.
107. Sholl, D. S.; Lively, R. P., Defects in Metal–Organic Frameworks: Challenge or Opportunity? *The Journal of Physical Chemistry Letters* **2015**, *6*, 3437–3444.
108. Chokbunpiam, T.; Fritzsche, S.; Caro, J.; Chmelik, C.; Janke, W.; Hannongbua, S., Importance of ZIF-90 Lattice Flexibility on Diffusion, Permeation, and Lattice Structure for an Adsorbed H₂/CH₄ Gas Mixture: A Re-Examination by Gibbs Ensemble Monte Carlo and Molecular Dynamics Simulations. *The Journal of Physical Chemistry C* **2017**, *121*, 10455–10462.
109. Freeman, B. D., Basis of Permeability/Selectivity Tradeoff Relations in Polymeric Gas Separation Membranes. *Macromolecules* **1999**, *32*, 375–380.
110. Zhao, P.; Lampronti, G. I.; Lloyd, G. O.; Wharmby, M. T.; Facq, S.; Cheetham, A. K.; Redfern, S. A. T., Phase Transitions in Zeolitic Imidazolate Framework 7: The Importance of Framework Flexibility and Guest-Induced Instability. *Chemistry of Materials* **2014**, *26*, 1767–1769.
111. Pilvar, P.; Fritzsche, S.; Caro, J.; Janke, W., Molecular Dynamics Investigation of the Transport of Hydrogen in ZIF-7. *Diffusion Fundamentals* **2013**, *20*, 1.
112. Wu, X.; Niknam Shahrak, M.; Yuan, B.; Deng, S., Synthesis and Characterization of Zeolitic Imidazolate Framework ZIF-7 for CO₂ and CH₄ Separation. *Microporous and Mesoporous Materials* **2014**, *190*, 189–196.
113. Rashidi, F.; Blad, C. R.; Jones, C. W.; Nair, S., Synthesis, Characterization, and Tunable Adsorption and Diffusion Properties of Hybrid ZIF-7-90 Frameworks. *AIChE Journal* **2016**, *62*, 525–537.
114. Remi, J. C. S.; Lauerer, A.; Chmelik, C.; Vandendael, I.; Terryn, H.; Baron, G. V.; Denayer, J. F. M.; Karger, J., The Role of Crystal Diversity in Understanding Mass Transfer in Nanoporous Materials. *Nat. Mater.* **2016**, *15*, 401–406.
115. Verploegh, R. J.; Wu, Y.; Boulfelfel, S. E.; Sholl, D. S., Quantitative Predictions of Molecular Diffusion in Binary Mixed-Linker Zeolitic Imidazolate Frameworks Using Molecular Simulations. *Journal of Physical Chemistry C* **2018**, *122*, 5627–5638.

- 1
2
3 116. Thornton, A. W., et al., Materials Genome in Action: Identifying the Performance Limits of
4 Physical Hydrogen Storage. *Chemistry of Materials* **2017**, 29, 2844-2854.
5 117. Witman, M.; Ling, S.; Jawahery, S.; Boyd, P. G.; Haranczyk, M.; Slater, B.; Smit, B., The
6 Influence of Intrinsic Framework Flexibility on Adsorption in Nanoporous Materials. *Journal of the*
7 *American Chemical Society* **2017**, 139, 5547-5557.
8 118. Pophale, R.; Cheeseman, P. A.; Deem, M. W., A Database of New Zeolite-Like Materials.
9 *Physical Chemistry Chemical Physics* **2011**, 13, 12407-12412.
10
11
12
13

TOC Graphic

